

Journal of Geophysical Research: Oceans

RESEARCH ARTICLE

10.1029/2018JC013786

Special Section:

Sea State and Boundary Layer Physics of the Emerging Arctic Ocean

Key Points:

- A unique shipboard air, ice, ocean data set describes the near-surface environment during the Chukchi/Beaufort Seas autumn freezeup
- Fall heat loss is important over both thin new ice and nearby open water, but relative cooling of over-ice air produces important feedbacks
- Ice drift and ocean thermohaline structure are impacted at certain times and locations by upper-ocean current and/or small-scale eddies

Supporting Information:

- Supporting Information S1

Correspondence to:P. O. G. Persson,
ola.persson@colorado.edu**Citation:**Persson, P. O. G., Blomquist, B., Guest, P., Stammerjohn, S., Fairall, C., Rainville, L., et al. (2018). Shipboard observations of the meteorology and near-surface environment during autumn freezeup in the Beaufort/Chukchi Seas. *Journal of Geophysical Research: Oceans*, 123, 4930–4969. <https://doi.org/10.1029/2018JC013786>

Received 12 JAN 2018

Accepted 22 MAY 2018

Accepted article online 12 JUN 2018

Published online 23 JUL 2018

Shipboard Observations of the Meteorology and Near-Surface Environment During Autumn Freezeup in the Beaufort/Chukchi Seas

P. Ola G. Persson^{1,2} , Byron Blomquist^{1,2} , Peter Guest³ , Sharon Stammerjohn⁴ , Christopher Fairall² , Luc Rainville⁵, Björn Lund⁶ , Stephen Ackley⁷, and Jim Thomson⁵ 

¹Cooperative Institute for Research in Environmental Sciences, University of Colorado Boulder, Boulder, CO, USA, ²NOAA/ESRL/Physical Sciences Division, Boulder, CO, USA, ³Department of Meteorology, Naval Postgraduate School, Monterey, CA, USA, ⁴Institute for Arctic and Alpine Research, University of Colorado Boulder, Boulder, CO, USA, ⁵Applied Physics Laboratory, University of Washington, Seattle, WA, USA, ⁶Center for Southeastern Tropical Advanced Remote Sensing, University of Miami, Miami, FL, USA, ⁷Snow and Ice Geophysics Laboratory, UTSA, San Antonio, TX, USA

Abstract The collection and processing of shipboard air, ice, and ocean measurements from the Sea State field campaign in the Beaufort/Chukchi Seas in autumn 2015 are described and the data used to characterize the near-surface freezeup environment. The number of parameters measured or derived is large and the location and time of year are unique. Analysis was done of transits through the new, growing ice and of ice edge periods. Through differential surface energy fluxes, the presence of new, thin sea ice (<50 cm) produces lower tropospheric air temperatures in the ice interior that average ~4°C colder than those over open water near the ice edge, resulting in an ice edge baroclinic zone. This temperature difference doubles by late October and produces thermodynamic and dynamic feedbacks. These include off-ice, cold-air advection leading to enhanced surface heat loss averaging ~200 W/m² over the open water, formation of low-level jets, suppression of the ice edge baroclinic zone, and enhanced ice drift. The interior ice growth rate is thermodynamically consistent with a surface heat loss of ~65 W/m² to the atmosphere and a heat flux of several tens of W/m² from the ocean below. Ice drift at times contributes to the southward advance of the autumn ice edge through off-ice winds. The ocean thermohaline structure is highly variable and appears associated with bathymetric features, small-scale upper-ocean eddies, and the growing ice cover. Lower salinity under the ice interior compared to the nearby ice edge is an upper-ocean impact of this thin ice cover.

Plain Language Summary The collection and processing of shipboard air, ice, and ocean measurements from the Sea State field campaign in the Beaufort/Chukchi Seas in autumn 2015 are described and the data used to characterize the air-ice-ocean environment during the autumn freezeup. Sampling the ocean freezeup process is unique, while the large number of parameters measured or derived allows for improved understanding of the interactions between the atmosphere, ice, and upper ocean. Analysis is done of transits through new, growing ice and of ice edge periods. The formation of new, thin sea ice (<50 cm) quickly produces near-surface air temperatures over the ice that are significantly colder than those over open water near the ice edge, leading to features such as an off-ice flow of cold air that greatly enhances the heat loss from the nearby open water, strong winds near the ice edge, and enhanced ice drift. The thermal and salinity structure of the upper ocean is highly variable and appears associated with bottom topography, upper-ocean eddies, and the growing ice cover. These results will improve the understanding of air-ice-ocean interactions and permit the validation of coupled air-ice-ocean models now being developed.

1. Introduction

The Northern Hemisphere September sea ice extent has decreased by over 40% since 1979 (e.g., Stroeve et al., 2012; National Snow and Ice Data Center), leaving new, large areas of open water around the periphery of the Arctic Basin at the end of the summer melt season along with remnant ice surviving the summer in the Central Arctic, defined here as multiyear ice (MYI). The minimum in sea ice extent occurs in mid-September. During the autumn after mid-September, the ocean loses heat until it reaches its freezing point, at which time ice starts forming. This thin, growing ice represents new first-year ice (FYI). From satellite imagery, such as ice concentration imagery from AMSR2 (Spreen et al., 2008), this freezeup appears as a movement of ice extent southward from the mid-September edge of the MYI, though most of this new ice does not represent the

southward advection of ice but rather the growth of thin FYI. This autumn period of ocean cooling and ice advance/growth has rarely been sampled with in situ measurements, so the measurements from the R/V *Sikuliaq* during the Sea State field campaign in autumn 2015 represent a unique data set.

Extensive atmospheric measurements over relatively thick sea ice have been made several times during the late summer from cruises of the Swedish icebreaker R/V *Oden* (e.g., Tjernström et al., 2004, 2012, 2015) and cruises by the German icebreaker R/V *Polarstern* (e.g., Lüpkes et al., 2010). Even the extensive atmosphere, ice, and ocean data collected during the 1-year drift of the SHEBA ice camp in 1997–1998 (e.g., Persson et al., 2002; Uttal et al., 2002) does not represent conditions over open water and thin, growing FYI. Measurements from the Japanese research vessel R/V *Mirai* have captured the atmospheric and surface conditions during the onset of the ocean cooling in late September in the Chukchi Sea (e.g., Inoue & Hori, 2011, Inoue et al., 2014), but has never made measurements during the period of ocean freezeup since it is not an ice-capable ship. The cruise of the R/V *Oden* in 2014 also captured ocean cooling and a few days of the incipient stages of ocean ice growth in late September (Sotiroopoulou et al., 2016) but left the area before extensive measurements were obtained.

Numerous air-ocean interaction studies have been carried out, investigating energy fluxes, turbulent fluxes, lower atmosphere impacts, and upper-ocean impacts, including impacts of and on waves (e.g., Edson et al., 2014; Fairall, Bradley, Rogers, et al., 1996; Fairall et al., 2003; Persson et al., 2005) and studies in the Chukchi-Beaufort Sea region (e.g., Kawaguchi et al., 2015; Waseda et al., 2018). Air-ice-ocean interactions not only increase the number of substrates to be described but also triples the number of interfaces across which fluxes occur. Hence, the complexity of air-ice-ocean interactions is greatly increased over air-ocean, ice-ocean, and air-ice interactions individually. Previous meteorological, upper-ocean, and ice measurements in this air-ice-ocean environment have typically consisted of buoy measurements with limited atmospheric, ocean, and surface parameters (e.g., Lee et al., 2017) and focused on details of a specific process (e.g., Fairall & Markson, 1987; Smith & Thomson, 2016). Some aircraft studies have examined the structure of the atmospheric boundary layer over the autumn sea ice and adjacent open water (e.g., Paluch et al., 1997; Pinto, 1998), but these have very limited or no measurements of the upper ocean or ice conditions. Clearly, studies are needed to show the lower tropospheric and upper-ocean structure in relationship to the surface ice and open water characteristics in a variety of atmospheric and ocean forcing conditions. Such studies should include heat and momentum fluxes across the interfaces and other interaction processes. The description of these structures, fluxes, and processes are clearly needed, especially at a time of year when significant spatial variability exists and the lower atmosphere, upper ocean, and sea ice are rapidly evolving, such as during autumn freezeup.

This study will describe the environment of the lower troposphere, upper-ocean, and the associated ice/ocean surface during the freezeup of the Beaufort and Chukchi Seas as measured from the R/V *Sikuliaq* during the Sea State cruise in autumn 2015. The description of the large suite of measurements and the data processing done to produce a high-quality data set is presented first. Measurements were made with a variety of instruments, making this data set unique for representing the freezeup environment with its broad range of parameters. This description is of particular use to studies utilizing these measurements for more in-depth processes analyses. The evolving sea ice cover relative to the ship track and synoptic/mesoscale weather are key forcings for the observed lower-troposphere and upper-ocean conditions. These are described in section 3 and are crucial for understanding the near-surface meteorological and ocean conditions that are subsequently described. The bathymetry of the Sea State area relative to the ship observations is also described, as the observations also suggest that it likely plays a role in determining the structure of at least the upper ocean. Because measurements were obtained both in open water areas adjacent to the growing ice and in the forming FYI itself, the cruise is divided into four ship transits through the ice interior and four ice edge periods when the ship was quasi-stationary near the ice edge. The analyses focus on juxtaposition of the lower atmosphere, surface, and upper-ocean conditions in order to suggest the interactive processes. As will be shown, the presence of ice is a key modulator of environmental conditions. This paper focuses on a broad environmental description, suggesting relationships between atmospheric and oceanic structure and the surface conditions, rather than on details of various interaction processes. Detailed analyses of key processes unique to this environment are left to subsequent studies. The uniqueness of this study is its characterization of the rarely sampled environment through the extensive number of parameters measured, rather than in-depth process analysis.

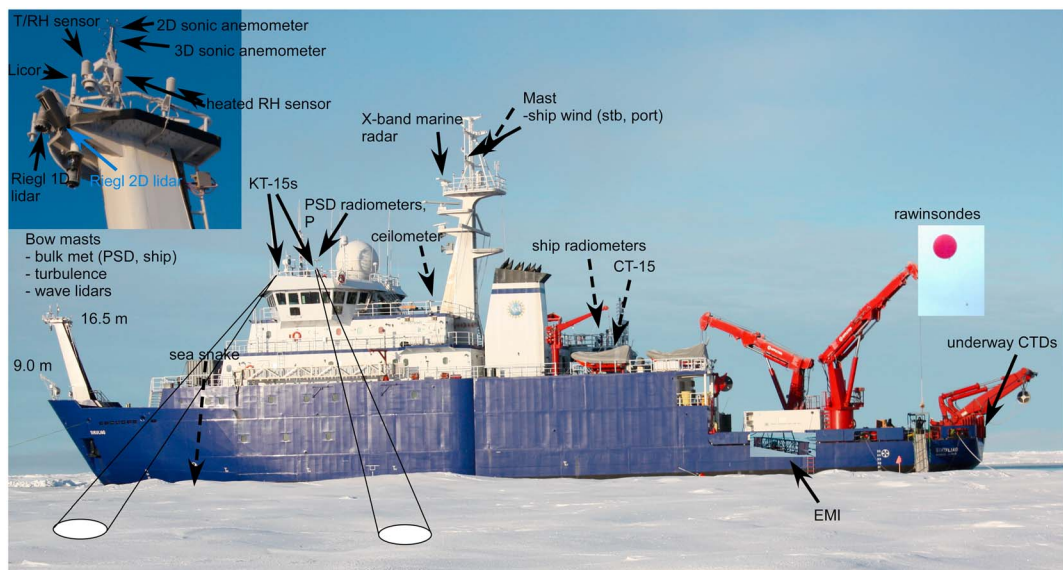


Figure 1. Locations of key meteorological, surface, and upper-ocean instrumentation on the R/V *Sikuliaq* during the Sea State cruise. Solid arrows indicate locations visible in the image; dashed arrows indicate locations on the starboard side of the ship and hence not visible. Insert shows top of bow mast. The fields of view of the KT-15 radiometers are indicated by the beams emanating from the bridge. See text and Tables 1–3 for more details.

2. Measurements and Data Processing

During the Sea State campaign, many continuous air, ice, and ocean measurements were made from a variety of sensors located at different locations on the R/V *Sikuliaq* (Figure 1). Some parameters were directly measured, while others were derived. The sensors, sampling rates, and sensor locations for the continuously measured parameters are specified in Tables 1–3 below, with the sources, methodology, and references for the derived parameters described in Table 4. This section summarizes some of the considerations for the direct measurements, the data processing and quality control involved in producing the directly measured parameters, and the techniques involved in producing the derived parameters. More details of the measurements and data processing are provided in the supporting information Texts S1 and S2. Only shipboard continuously measured, derived parameters, and upper-air rawinsonde data are considered here. Sea State special measurements during intensive observing periods, such as wave buoy deployments or ice stations, are not included in this discussion. Furthermore, measurements from satellites, aircraft, or remotely operated vehicles are mostly not described here, except for a few satellite parameters needed to place the Sea State cruise in spatial and temporal context.

2.1. Directly Measured Meteorological and Air-Surface Flux Parameters

Basic meteorological parameters, such as air temperature (T_a), specific and relative humidity with respect to water and ice (q_a , RH_w , RH_i), air pressure (p), and wind speed/direction (ws/wd) were measured at the 15.4–16.5-m height above mean sea level (MSL) on the bow mast, on the bridge roof at ~17 m MSL, and on the main mast at ~25 m MSL (Table 1). Direct calculations of turbulent fluxes, utilizing covariance and inertial dissipation methods, were made from the bow mast and davit-supported sensors at heights of 9.0 and 16.5 m MSL, while rapid measurements of q_a at 15.4 m height support calculations of latent heat fluxes. Tropospheric profiles of pressure, temperature, and wind were obtained with rawinsondes launched every 3–6 hr from the fantail of the ship and with greater frequency for specific periods of interest, such as in zones of strong atmospheric gradients near the ice edge. The launch methodology was frequently modified by inducing a leak in the balloon to obtain data during both balloon ascent and descent in the lowest ~3 km. Cloud information was obtained through a ceilometer, providing cloud base and cloud fraction, and humidity measurements from the rawinsondes. Cloud top heights are estimated from the soundings as the highest level above cloud base for which $RH_w > 95\%$. Downwelling shortwave (SW_d) and longwave (LW_d) radiation were measured from two Eppley Precision Solar Pyranometers (PSPs) and two Eppley Precision Infrared Radiometers (PIRs)

Table 1

Sensors for Shipboard Atmospheric Measurements, Including Turbulence and Downwelling Radiation

Parameter measured	Sensor	Sampling rate	Location; height above surface
p (PSD)	Vaisala PTB 220	5 s (1 min average)	bridge roof; 17 m
ws, wd (PSD)	Metek uSonic-3	20 Hz	bow mast; 9.0, 16.5 m
T_a, RH_a (PSD)	Vaisala HMT355, 337	5 s (1 min average)	bow mast; 15.4 m
p (ship)	Vaisala PTU307	5 s	bow mast; 16.5 m
ws, wd (ship)	Gill WindObserver 75	1 Hz	bow mast; 16.2 m
T_a, RH_a (ship)	2-D sonic RM Young 85000	4 Hz	main mast (prt, stbd); 25 m
p, T_a, RH_a, ws, wd	Vaisala PTU307	5 s	bow mast; 15.4 m
u', v', w', T_v' , τ , H_s	Vaisala RS92 rawinsondes	3–6 hr (2 s)	fantail; 3 m–15,000 m
q_d', CO_2', H_2	Metek uSonic-3	20 Hz	bow mast; 9.0, 16.5 m
p, p'	Licor 7500	10 Hz	bow mast; 15.4 m
Cloud base/freq.	Paro Scientific 6000	10 Hz	bow mast; 9.0, 16.5 m
LW_d, SW_d (PSD)	Vaisala CT25K ceilometer	15 s	deck 4; ~14 m–7,600 m
LW_d, SW_d (ship)	Eppley PIR(2)/PSP(2)	5 s (1 min)	bridge roof; 17 m
	Eppley PIR/PSP	5 s	midships, deck 3; ~12.5 m

Note. Perturbation values of three-dimensional wind components (u, v, w), virtual temperature (T_v), and absolute humidity (q_d) are used in turbulent flux calculations and are marked by '.

mounted on the bridge roof. Measurements of some of the basic meteorological parameters and the downwelling broadband radiation were also provided by ship-operated sensors (labeled *ship* in Tables 1 and 2). Careful comparisons between the ship sensors and those deployed by National Oceanic and Atmospheric Administration/Physical Science Division (PSD) were made in quality control assessments.

Measurements of atmospheric parameters, including basic state parameters, can be strongly influenced by air flow deformation and *heat island* effects when made on board a ship, as well as by processes associated with this unique Arctic environment, such as instrument riming. Detailed monitoring and documentation during the cruise and careful comparisons between apparent redundant measurements were done to identify these effects and to determine how best to combine the various measurements to obtain a high-quality data set. Key results from these comparisons described in more detail in the supporting information or by Blomquist et al. (2015) include the following:

Table 2

Sensors for Shipboard Measurements of Ocean and Ice Surfaces

Parameter measured	Sensor	Sampling rate/scale	Sensor location/Sampling area
T_s (PSD)	Heitronics KT-15 (2)	1 Hz	Bridge roof; 25–30 m to port
T_{sn}	Floating thermistor (sea snake)	5 s (1 min)	Bridge, 2–4 m to starboard, 5 cm depth
T_s (ship)	Heitronics CT-15	5 s	Midship, deck 2; 3–4 m to starboard
Salinity (S ; ship)	Thermosalinograph SBE45	5 s (1 min)	Midship, 6.5 m depth
Ocean sfc freezing point, T_{frz}	Thermosalinograph SBE45	5 s (1 min)	Reference
Sig wave height; wave outline	1-D Riegl LD90 lidar	10 Hz	Bow mast; 3–4 m forward of bow
Sig wave height; wave outline	2-D Riegl LMS-Q240i scanning lidar	20 Hz	Bow mast; 3–4 m forward of bow
Peak wave period	Rutter marine X-band radar	5 min (1.25 s)	Main mast; 7.5 m res., 4 km range
Peak wave direction	Rutter marine X-band radar	5 min (1.25 s)	Main mast; 7.5 m res., 4 km range
Sfc current speed	Rutter marine X-band radar	5 min (1.25 s)	Main mast; 7.5 m res., 4 km range
Sfc current direction	Rutter marine X-band radar	5 min (1.25 s)	Main mast; 7.5 m res., 4 km range
Ice conc, total-ASSIST	Manual observer	60 min	Bridge; ~1 km range
Ice thick, primary-ASSIST	Manual observer	60 min	Bridge; ~1 km range
Ice type, primary-ASSIST	Manual observer	60 min	Bridge; ~1 km range
Snow depth-ASSIST	Manual observer	60 min	Bridge; ~1 km range
Floe size, primary-ASSIST	Manual observer	60 min	Bridge; ~1 km range
Ice thick – dipnet, thk_{dpn}	Manual dipnet/ruler	Irregular	Fantail, starboard
Ice thick-EMI	Geonics EM31	1 Hz, Irregular	Fantail, 6 m to port
Surface backscatter	Rutter marine X-band radar	5 min (1.25 s)	Main mast; 7.5 m res., 4 km range

Note. ASSIST = Arctic Shipborne Sea Ice Standardization Tool; EMI = ElectroMagnetic Induction.

Table 3
Shipboard Sensors for Upper Ocean Measurements

Parameter measured	Sensor	Sampling rate/scale	Sensor location/Sampling area	Accuracy
Temperature, salinity (T_o , S)	Teledyne Ocean science underway CTD	16 Hz, ~11 min (4,325 uCTDs in 32 days)	stern; 4 m–150 m depth	T : 0.004 °C S : 0.05 psu D : 1 dbar

Note. uCTD = underway conductivity-temperature-depth.

1. The air pressure at 17 m is the mean value of the PSD PTB220 and the ship PTU307 sensors. It is then height adjusted to produce the mean sea level pressure (MSLP).
2. Air temperatures (T_a) from the HMT337 are used for this study, but values from any of the other sensors, which all agree within 0.2°C, are used if HMT337 data are missing (very rare).
3. RH_w measurements from the HMT337 are used in this study, with any gaps filled with those from the HMT335.
4. Because the PSD anemometer is higher and farther from the top of the bow tower than the ship anemometer, its value is used in this study for ship-relative wind direction (WD_{rel}) within ±120° of bow-on. When WD_{rel} exceeds ±120°, the main mast anemometer for the windward side is used.
5. Instrument riming was the major problem for accurate downwelling radiation measurements during Sea State, as T_a was below freezing, the RH was high, supercooled fog drops were frequently observed, and even sea spray occurred on a few occasions with strong winds over open water. Riming can produce up to a ~40–80 W/m² positive error for a given LW_d value, but it is nearly impossible to discern whether riming is occurring from the LW_d measurement itself.

The six radiometers on the R/V *Sikuliaq* were manually cleaned several times per day, and a careful log was kept of the degree of riming during each visit. This information was used to edit and correct the downwelling radiation data as described in the supporting information Text S1. Linear interpolation was done between remaining *good* data. The degree of riming and impact of the riming on the measurements varied with conditions. A period of severe riming occurred from 20 to 24 October (DoY 293–297; see Figure S1), which included a few days of clear skies. The 5-day mean edited LW_d of 218.1 W/m² is 9.5 W/m² less than the mean of the unedited data, though individual 10-min points decrease by up to 50 W/m². Other time periods were not as strongly impacted by riming as this period, and mean changes due to the editing were hence less.

Downwelling shortwave radiation (SW_d) was also manually edited based on the observed degree of riming at the time of cleaning, and linear interpolation was also done between the remaining *good* values. Zero values were inserted whenever the solar zenith angle was greater than 90°. The impact of editing on SW_d was

Table 4
Air-Ice-Ocean Parameters Derived From Shipboard Measurements

Parameter	Data frequency/resolution	Source or reference
Atmospheric mixed-layer height (AMLH)	3–6 h	Rawinsondes; see text
LW _u	1 Hz, ~3–5 m	T_{skn} , KT-15 (2); see text
SW _u	1 Hz, ~3–5 m	T_{skn} , KT-15 (2) (Perovich & Polashenski, 2012)
Bulk turb fluxes (τ_b , H_{sb} , H_{lb})	10 min (1 s)	Persson et al. (2002), Fairall et al. (2003); see text
Net sfc energy flux, F_{atm}	10 min	$F_{atm} = SW_d - SW_u + LW_d - LW_u - H_{sb} - H_{lb}$
Ice thick-SEB, thk _{SEB}	1 Hz, ~3–5 m	T_{skn} , KT-15 (2); see text
Ice conc-SEB, IC _{SEB}	10 min, ~1.2–3.0 km	T_{skn} , KT-15 (2); see text
Ice drift speed	30 min	Backscatter, marine radar (Lund et al., 2017)
Ice drift direction	30 min	Backscatter, marine radar (Lund et al., 2017)
Ice conc-satellite	Daily, 3.1 km	AMSR2 (Spreen et al., 2008)
Ocean mixed-layer depth	~11 min, to 150 m, 1 m res	uCTDs; see text
Ocean mixed-layer heat content	~11 min, to 150 m, 1 m res	uCTDs; see text?
T_{frz} ; ocean freezing point	~11 min, to 150 m, 1 m res	from S using Fofonoff and Millard (1983)
T_{oxcs} ; ocean excess temp	~11 min, to 150 m, 1 m res	$T_O - T_{frz}$

Note. SEB = surface energy budget; uCTD = underway conductivity-temperature-depth; AMSR2 = Advanced Microwave Scanning Radiometer 2.

significantly smaller than for LW_d because clear-sky midday values of SW_d were $< 150 \text{ W/m}^2$ for the campaign and frequently $< 50 \text{ W/m}^2$. For both LW_d and SW_d , we use the median values of the manually edited, 10-min mean, downwelling radiation from each of the two pairs of PSD radiometers, with or without the missing data filled in through linear interpolation between good data points. The former is considered the best data set. The ship radiometer values are not used in this study.

Direct measurements of turbulent flux parameters are only possible when WD_{rel} is between $\pm 90^\circ$ from bow-on. Furthermore, if the ship is moving too rapidly ($sog > 3 \text{ m/s}$), these direct techniques also produce questionable results. During Sea State, only about 46% of the 10-min time periods had a WD_{rel} and ship speed meeting the above criteria and hence suitable for calculation of turbulent momentum and sensible heat fluxes from covariance and inertial dissipation techniques. Furthermore, flux stations, defined as when the ship was nearly stationary ($sog < 1 \text{ m/s}$) for at least 50 min and oriented into the wind ($|WD_{\text{rel}}| < 45^\circ$) the entire time, provided even higher-quality turbulent fluxes. Good 10-min flux values were obtained over near 100% ice cover (thin, growing FYI), over open water near the ice edge, and over a surface of mixed ice and open water with various ice concentrations.

An unheated Licor 7500 sensor was mounted on the bow tower for calculating direct fluxes of latent heat, but riming caused major data losses. Good latent heat fluxes were collected in only $\sim 8\%$ of the 10-min periods, exclusively in areas of warmer temperatures, where not only the ship orientation and speed criteria were met but also when riming did not eliminate useful data.

2.2. Surface Parameters

Shipboard measurements of parameters describing the ice and ocean surface conditions were obtained through both sensors and manual methods (Table 2). The surface or *skin* temperature (T_s) is an important parameter, so was measured by three techniques during Sea State. These include a precision thermometer epoxied into a brass plug in the end of a floating, sealed tygon tube measuring the temperature at $\sim 5\text{-cm}$ depth for water surfaces (*sea snake*; Fairall et al., 1997), two KT-15 infrared thermometers, and one CT-15 infrared thermometer (see Figures S2a–S2c). The KT-15 sensors were mounted on the bridge roof, portside, railing about 4 m apart, with the forward one pointed slightly forward and the aft one slightly aft. This resulted in $\sim 3\text{-m}$ wide sampling spots about 24 m apart in the along-ship direction $\sim 25\text{--}30 \text{ m}$ from the portside of the ship, outside the ship's wake (see Figure 1). The lenses of the two KT-15 IR thermometers were cleaned at the same time as the broadband radiometers, and manual editing of the data was done using guidelines specified in the supporting information Text S2. The CT-15 was mounted closer to the surface, sampling a spot only $\sim 3 \text{ m}$ from the starboard side of the ship. The long barrel protecting its lens made it very difficult to clean and to evaluate its riming status; however, the data suggest that riming occurred significantly less frequently for this instrument.

The processing of the KT-15 temperatures includes correction for the measured internal temperature and for the reflected longwave radiation. Comparisons between edited T_s data from the various sensors show absolute biases of $< 0.3^\circ\text{C}$ and root-mean-square error of $\sim 0.3\text{--}1.1^\circ\text{C}$ (see supporting information Text S2). The cool-skin effect is removed from the sea snake temperature (Fairall, Bradley, Godfrey, et al., 1996), improving the absolute bias and root-mean-square error comparisons by $\sim 0.2^\circ\text{C}$. Comparisons to the freezing point of the seawater (T_{frz}) computed from the measured salinity (see below) for times when the observed T_s is within 1°C of T_{frz} and the ship is in open water but very near the ice edge (assumed to represent an ice bath), determine biases that were used to correct the KT-15 and CT-15 data. A *best* radiometric skin temperature, T_{skn} , was then assumed to be the mean of the corrected values from the three radiometric sensors when the ship was stationary, since the three sensors then all measured different surface spots. When the ship was moving, the radiometric sensor most different from the air temperature (T_a) was used for T_{skn} , since each sensor should sample a similar surface and differences are in this case likely due to unmitigated riming rather than true spatial variability. After the above corrections, we estimate that the mean T_{skn} is accurate to $\pm 0.1^\circ\text{C}$, with individual measurements accurate to $\pm 0.3^\circ\text{C}$. No correction was made to the sea snake temperature (T_{sn}), though the above analysis suggests it may be 0.2°C too warm.

The near-surface salinity is obtained from the ship's thermosalinograph, which has an intake at $\sim 6\text{-m}$ depth. Since the temperature sensor at the intake was not functional, temperature and conductivity measurements were made in the main lab of the ship, resulting in measured water temperatures that are too warm by an

average of 1.2°C. The salinity, which is computed from the measured conductivity and temperature, is determined by recalculating the conductivity from the incorrect measured temperature and salinity and then recomputing the salinity from the conductivity using an improved water temperature. The water temperature used was either the measured (and corrected) sea snake value or the corrected T_{sCT15} value if these were above -1.6°C (indicating open water) or the maximum of -1.6°C and a correction to the thermosalinograph with the above bias at other times (indicating that the water sample was taken below ice). This revised salinity value is on average 1.2 psu greater than the one directly measured by the thermosalinograph. It is then used to calculate T_{frz} from Fofonoff and Millard (1983).

Ocean wave characteristics were measured from the ship by Riegl lidars mounted near the top of the bow mast and by a marine X-band radar mounted on the main mast of the ship. The 1-D Riegl lidar provided a distance to the ocean surface, which was combined with ship-motion measurements to obtain wave heights at 10 Hz temporal resolution. 10-min significant wave heights are computed as 4 times the square root of the zeroth moment of the motion-corrected wave height spectra (moment technique) and as 4 times the standard deviation of the measured surface height displacements (*CF* method). The first method is more accurate but requires that at least 50% of the samples during the 10-min time period are available, while the latter can obtain reasonable values with more missing data. Low infrared reflectivity of smooth water and ice surfaces and possibly icing on the lidar optics were the major reasons for missing data. Peak wave periods can be computed from the 1-D lidar spectra by applying phase correction based on the dominant wave direction, determined from the marine radar (Lund et al., 2017), and the ship motion using the technique described by Collins et al. (2017). Data from a 2-D lidar (Riegl LMS-Q240i), also mounted to the foremast, are currently being analyzed and are not used in this study. The marine X-band radar completed full scans every 1.25 s, providing backscatter fields with 7.5-m range resolution out to an effective range of ~ 4 km (Lund et al., 2018). The resolved waves are evident in these backscatter fields, providing estimates of peak wave periods, peak wave direction, surface current speed, and surface current direction every ~ 5 min using data-processing techniques described by Lund et al. (2017).

During Sea State, surface ice parameters from the ship are provided by a combination of manual and sensor observation techniques. The direct manual techniques include hourly visual observations from the ship's bridge using the Arctic Shipborne Sea Ice Standardization Tool (ASSIST) protocol (Hutchings, 2018); <http://www.climate-cryosphere.org/media-gallery/881-icewatch-assist>, which provided ice types, and estimates of their partial concentrations, the total ice concentration (IC_A), ice thickness (thk_A), snow cover depth, and floe sizes. The area viewed by the observers was limited to the nearest ~ 2 -km range during daylight hours and to the ship vicinity illuminated by a floodlight during night. Observers were trained prior to the cruise. These ASSIST estimates of ice thickness were supplemented by occasional shipside sampling of the ice cover retrieved manually with a dipnet and a frazilometer (thk_{dipn}). Thermodynamically derived ice thickness (IT_T) and ice concentration (IC_T) estimates are also computed, and satellite-based daily ice concentrations were collected, as described in section 2.4. Products from an onboard ElectroMagnetic Induction meter are still being processed and are hence not used in this study. Comparisons and assessments of the various measurement techniques for ice concentration and ice thickness are of interest but beyond the scope of this study.

2.3. Upper-Ocean Parameters

In addition to the surface temperature and salinity at 6.5-m depth described above, 4,325 upper-ocean profiles of pressure, temperature, and salinity were obtained during Sea State from an underway conductivity-temperature-depth (uCTD; Rudnick & Klinke, 2007) system mounted on the stern of the ship (Figure 1 and Table 3). Since the CTD is unpumped, processing takes variable fall speed into account. On average, this system provided a profile every hour of the cruise, with much faster sampling (up to every minute) during specific surveys (e.g., the ice edge racetrack; section 5.3).

2.4. Derived Parameters

Numerous key parameters were derived from the direct measurements made from the R/V *Sikuliaq*, and are listed in Table 4.

An additional estimate of ice thickness is derived as a complement to the thickness estimates described above. Ten-minute average ice thicknesses are calculated from surface temperatures measured by the KT-15 IR thermometers. The measured skin temperature, wind, ocean freezing point, and energy fluxes

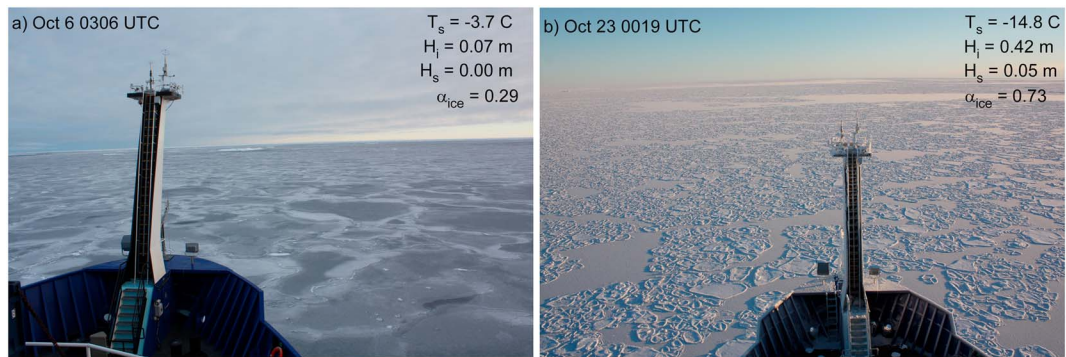


Figure 2. Photos showing two scenes for which the measured ice thickness and snow depth were used to estimate the ice surface albedo. Ice concentration is 91% for (a) and 100% for (b).

(see below) are combined with surface energy budget equations to estimate ice thickness over ~3-m wide spots (see Figure 1). This ship-based, surface energy budget (SEB) technique improves on related satellite-based algorithms used by Groves and Stringer (1991), Yu and Rothrock (1996), and Wang et al. (2010, 2016) and provides raw thickness estimates at 1-Hz temporal resolution (the temporal resolution of the KT-15 instruments). Hence, it also allows an estimate of ice concentration for each 10-min period nominally along a 1.8-km track, assuming a ship speed of 3 m/s. Ice concentration along the ship track is also obtained from the Advanced Microwave Scanning Radiometer 2 (AMSR2), which provides daily concentrations at 3.125 km resolution (Spreen et al., 2008). A mean ice concentration (A_i) is obtained by interpolating the ASSIST hourly estimates to the 10-min time intervals and then averaging the concentrations from the AMSR2, ASSIST, and SEB techniques. For thin ice, the AMSR2 concentrations are frequently smaller than those from the other techniques, so A_i are often slightly low estimates of ice concentration. Spurious ice concentrations over open water, which can result from weather effects on the AMSR2 retrievals (Guanghua & Jie, 2015; Spreen et al., 2008), were not noted along the ship track. This may be because no major storms with deep, moist clouds occurred during the cruise (see section 3).

Additional derived parameters describing the ice conditions include the ice drift speed and direction derived from the marine radar (Lund et al., 2018). The distance and direction to the nearest ice edge, and the ice edge orientation at that point are all derived from the ship's location and the AMSR2 ice concentration field. The ice edge is defined as the location of an ice concentration less than 15%.

Key surface parameters, such as albedo (α) and emissivity (ε), are determined by the surface type. For an open water surface, we assume $\varepsilon = \varepsilon_w = 0.99$ and $\alpha = \alpha_w = 0.08$. For an ice or snow surface, $\varepsilon = \varepsilon_i = 0.985$, but α depends on ice thickness and snow cover. Here we use the relationship of Maykut (1982) for bare ice albedo as a function of ice thickness, with the total ice albedo (α_{ice}) being a combination of the ice and snow albedo ($\alpha_{\text{snow}} = 0.85$) weighted by the snow fraction, which is determined from the snow depth as in Briegleb et al. (2004). The ice thickness used in this calculation is the mean of the four ice thickness estimates described above, while the only available snow depth is from the ASSIST observations. The total surface albedo is then calculated from

$$\alpha = A_i \alpha_{\text{ice}} + (1 - A_i) \alpha_w, \quad (1)$$

where A_i is the ice fraction. Figure 2 illustrates the application of this albedo scheme.

Using these parameters, the upwelling radiation (LW_u , SW_u) is determined from

$$LW_u = A_i [LW_d (1 - \varepsilon_i) + \varepsilon_i \sigma T_{si}^4] + (1 - A_i) [LW_d (1 - \varepsilon_w) + \varepsilon_w \sigma T_{sw}^4] \quad (2)$$

and

$$SW_u = A_i SW_d \alpha_i + (1 - A_i) SW_d \alpha_w, \quad (3)$$

where T_{si} and T_{sw} are the skin temperatures over the ice and water surfaces, respectively. If the net skin temperature (T_s) is below T_{frz} , it is assumed that $T_{sw} = T_{frz}$, and T_{si} is computed using the measured A_i . If it is above,

but $A_i > 0$, it is assumed that T_{si} is the linear interpolation between T_{frz} and 0°C using A_i , with $T_{sw} = T_{frz}$ plus additional heat if $T_s > 0^\circ\text{C}$.

Bulk turbulent fluxes are calculated separately over the ice and water portions of the scene, using the same atmospheric values for each. Over ice, the scheme used is the one from Persson et al. (2002) based on SHEBA measurements, but with the stability correction functions of Grachev et al. (2007). Over water, the COARE3.0 scheme (Fairall et al., 2003) is used but only with the Charnock and viscosity estimates of surface roughness and not the wave parameters. The net turbulent flux is then calculated by weighting each appropriately with the ice fraction, as given by

$$H_s = A_i H_{si} + (1 - A_i) H_{sw} \quad (4)$$

$$H_l = A_i H_{li} + (1 - A_i) H_{lw} \quad (5)$$

$$\tau = A_i \tau_i + (1 - A_i) \tau_w, \quad (6)$$

where H_s and H_l are the sensible and latent heat fluxes, respectively, τ is the stress, and X_i and X_w are the turbulent fluxes of X from the SHEBA and COARE schemes, respectively. This approach to bulk turbulence estimation is only marginally satisfactory, as neither the SHEBA scheme, developed for thick multiyear ice, nor the COARE scheme, developed for open-ocean conditions, are appropriate for this environment. Specifically, the surface roughness in this marginal ice zone environment is likely different than those for which these two schemes were developed. However, comparisons between this combination of the two bulk schemes with 10-min direct covariance fluxes shows reasonable agreement in the mean (see sections 4 and 5), though with significant scatter. Schemes such as that by Andreas et al. (2010), which uses an ice fraction-dependent roughness length or that of Lüpkes et al. (2012), which considers ice fraction, freeboard, and floe sizes, are likely more appropriate and are currently being tested. The reason they are not directly used here is because they were developed for thicker ice (greater freeboard) than is observed with this thin, growing ice during Sea State.

The net atmospheric energy flux, F_{atm} , is then calculated from the various observed and derived terms described above using

$$F_{atm} = SW_d - SW_u + LW_d - LW_u - H_s - H_l. \quad (7)$$

F_{atm} is the total heat exchange between the surface and the atmosphere and is a key parameter.

The atmospheric mixed-layer height (AMLH) for each sounding was calculated as the lowest height at which the vertical gradient in virtual potential temperature (θ_v) becomes greater than $1^\circ\text{C}/110\text{ m}$ over a layer at least 100-m thick. To avoid artificial inversions caused by the ship's heat island or stack plume, this algorithm only considers heights of 100 m or more.

2.5. Upper-Ocean Structure

The temperature and salinity structure in the uppermost 150 m of the ocean was documented during the Sea State cruise by 4,325 underway CTDs. These were obtained using a winch from the stern of the ship (see Figure 1). At least the top 3 m of the data are likely contaminated by the ship and are not used. The ocean mixed-layer depth (OMLD) for each uCTD was computed by finding the top depth that had a potential density that was at least 0.2 kg/m^3 greater than the mean density in the top 10 m (e.g., Steele et al., 2011). The ocean freezing point (T_{frz}) and ocean excess temperature ($T_{oxcs} = T_o - T_{frz}$) are calculated from salinity by standard relationships (Fofonoff & Millard, 1983).

3. Key Large-Scale Characteristics

The near-surface atmospheric and oceanographic environment is hypothesized to be primarily forced by the presence of sea ice and by the synoptic or mesoscale weather (MSLP field, winds, large-scale thermal advection). The description of these two large-scale components provides the foundation for understanding the spatial and temporal variability of the near-surface meteorological and ocean conditions to be described in subsequent sections.

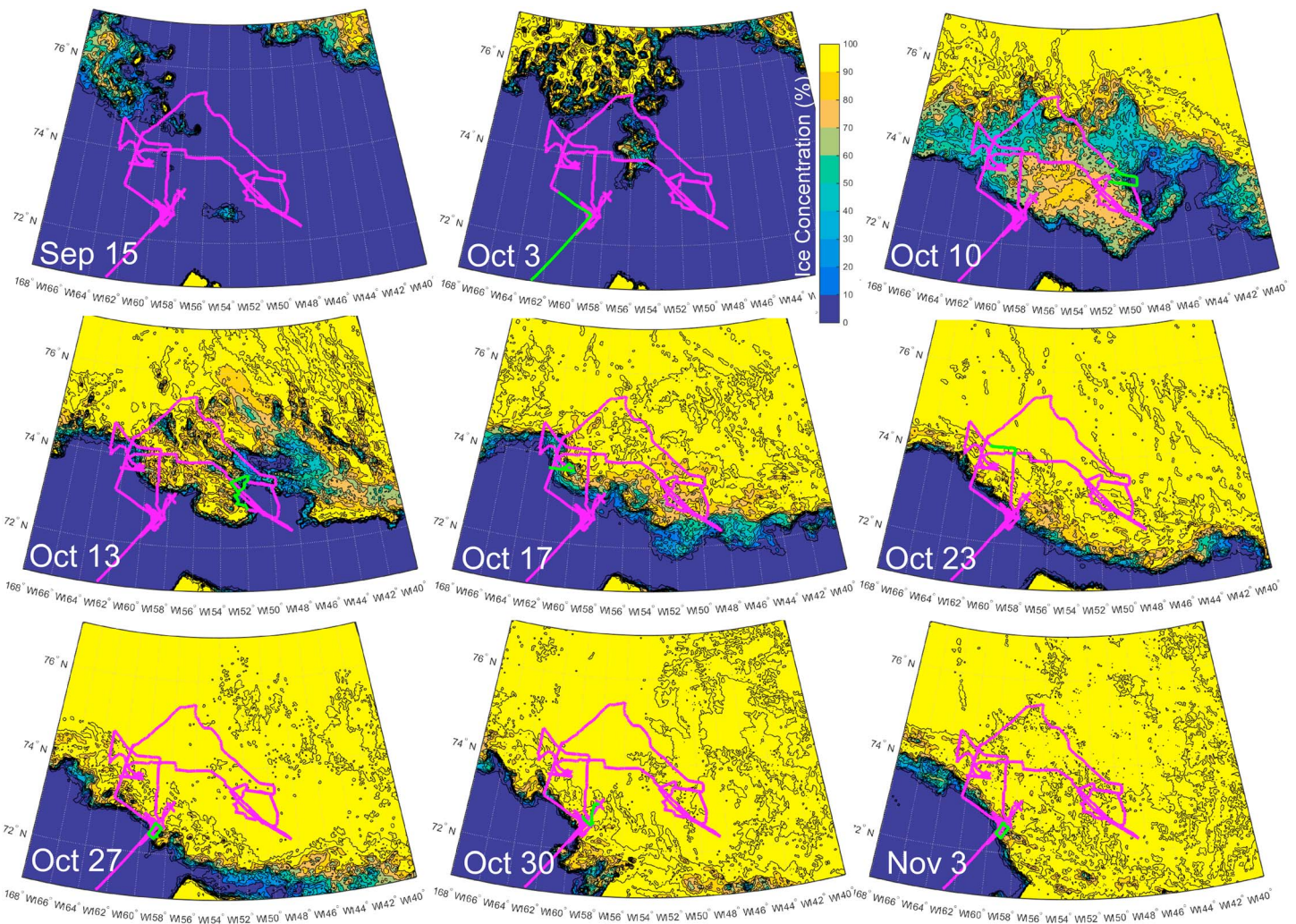


Figure 3. Ice concentration in the Sea State area in the Beaufort and Chukchi Seas on 15 September and on select dates during the Sea State cruise between 3 October and 4 November 2015. The magenta line shows the entire Sea State cruise track, while the portion highlighted in green shows the track for the same day as the AMSR2 concentration field. The small yellow area at the bottom of each panel is the northern tip of Alaska (Barrow).

3.1. Sea Ice Evolution and the Cruise Track

The Sea State field measurements were made in an approximately $400 \text{ km} \times 500 \text{ km}$ area of the Beaufort and Chukchi Seas centered near $74^\circ\text{N}, 156^\circ\text{W}$ directly north of Barrow, AK. In mid-September, this area was nearly devoid of ice, with only a few small remnant MYI floes in the northwestern portion of this domain (Figure 3a). By 3 October when the R/V *Sikuliaq* first reached the Sea State domain, some growth of FYI had begun, which continued and rapidly covered much of the Sea State cruise track with thin ice within a week (Figure 3c; also, see Figure 2a). A strong wind event on 10–13 October temporarily reduced the ice cover extent (Smith et al., 2018), though ice growth continued after this event. By 23 October, the edge of the expanding ice had reached the shelf break north of AK, having expanded southward 200 km in 20 days on the western side of the domain and 650 km southward on the eastern side. Only a narrow 50- to 80-km channel of open water remained between the sea ice and the growing landfast ice along the Alaskan Beaufort Sea coast. During the remaining 12 days of the Sea State cruise, growing ice slowly filled in this channel in the Beaufort Sea. In the Chukchi Sea, the sea ice advanced only slowly southward into relatively warm waters, advancing about 20–50 km in these 12 days.

The ship entered the growing thin FYI on 4 October and remained within high ice concentration until 10 October, sampling a few of the remnant MYI floes on 6–8 October in the northwestern part of the domain

(see Figure 3). On 10–13 October, the ship remained near the ice edge, deploying wave buoys as the ice regressed due to the effects of the strong on-ice wind event. On 14–16 October, the ship then continued back into the high-concentration, thin FYI, making measurements and sampling at additional ice stations. By 17 October, the ship had reached the western edge of the thin FYI, where additional ice sampling and wave buoy deployments were made. On 19–22 October, the ship then continued north and then east into very high concentration and thicker FYI, making atmospheric flux and ice sampling measurements, some by walking on the surface of the FYI. A transit to the ice edge was done on 23 October, crossing into open water at the time when moderately strong along-ice winds were occurring at the edge.

During 24–27 October, a rectangular *racetrack* (34.1 km × 18.5 km) was established and frequently repeated while deploying and recovering wave buoys. The ice edge often advanced and then retreated over the racetrack during this time period. Between 28 and 31 October, the ship again went about 100 km into the interior of the high-concentration FYI just north of the racetrack and performed several ice stations, returning to the ice edge and racetrack on 31 October. During the remainder of the cruise until departing the area late on 4 November, the ship continued deploying wave buoys, making atmospheric flux measurements, and sampling near and under the growing ice floes while making circuits around the racetrack. The ice edge continued to advance and retreat in response to the changing wind and atmospheric conditions, likely modulated by the upper-ocean heat content. Strong, obliquely off-ice winds dominated during 2–4 November, with ice generally advancing during this time period.

The daily 3.125-km AMSR2 ice concentrations along the ship track (e.g., Figures 3, 7, 13, 15, 18, 20, and 22) are used to help characterize the local surface conditions impacting the 10-min shipboard meteorological and oceanographic data to be described.

3.2. Synoptic/Mesoscale Weather Evolution

The synoptic weather pattern during the Sea State campaign was dominated by high pressure, which propagated through the Chukchi/Beaufort Seas region (Figure 4). The orientation of the high-pressure systems varied, though they tended to be located over the sea ice. The pressure gradient between these highs and the occasional low-pressure system that propagated eastward to the south in the Bering Strait region and across central Alaska produced significant winds (10–18 m/s), generally over the open water regions south of the ice edge. Five of the six examples of high-pressure dominance in Figure 4 produced such winds over the open water; three of these significant wind events (Figures 4b, 4d, and 4f) were sampled at the ice edge by the R/V *Sikuliaq*. The weather conditions for three of the excursions into the interior of the pack ice were dominated by high pressure and weak winds over the ice (Figures 4a, 4c, and 4e).

No strong surface cyclones (i.e., low-pressure centers or *storms*) occurred during Sea State. Even though three significant wind events were sampled by the R/V *Sikuliaq*, all of these were associated with predominant high pressure in the Sea State region, though the pressure gradient was enhanced over the near-ice open water. The Sea State measurements were briefly influenced by two weak and relatively small low-pressure systems on 14–15 October and 31 October (Figure 5). These both developed near the coastline of the Chukchi Sea and propagated to the northeast, were sufficiently small (~300–400 km) to be considered mesocyclones, and neither produced strong surface winds.

4. Lower-Atmosphere and Upper-Ocean Conditions During Ice Transits

Four transits from the ice edge, through the ice interior, and back to the ice edge were conducted by the R/V *Sikuliaq* (Figure 6). These are convenient segments to illustrate the interactions between the air, ice, and ocean over the thin new ice and nearby open water at this time of year. Here we use the term *ice edge* to indicate the transition zone from a few kilometers outside the first sighting of an ice *patch* to an area where the ice concentration (*Ai*) is consistently at a high value near 70%–100%, which is a less strict definition than that used for AMSR2 data in section 2.4. Shipboard measurements of the lower troposphere, sea ice, and upper ocean during these transits show the basic structure and structural variability associated with the changing ice conditions. This section shows data from these transits that illustrate the primary structural variability noted throughout the cruise. The next section describes the observations during four periods when the ship was quasi-stationary near the ice edge. These ice edge locations are shown by the red portions of the ship track in Figure 6. When examining the observations in both sections, it is important to keep in mind

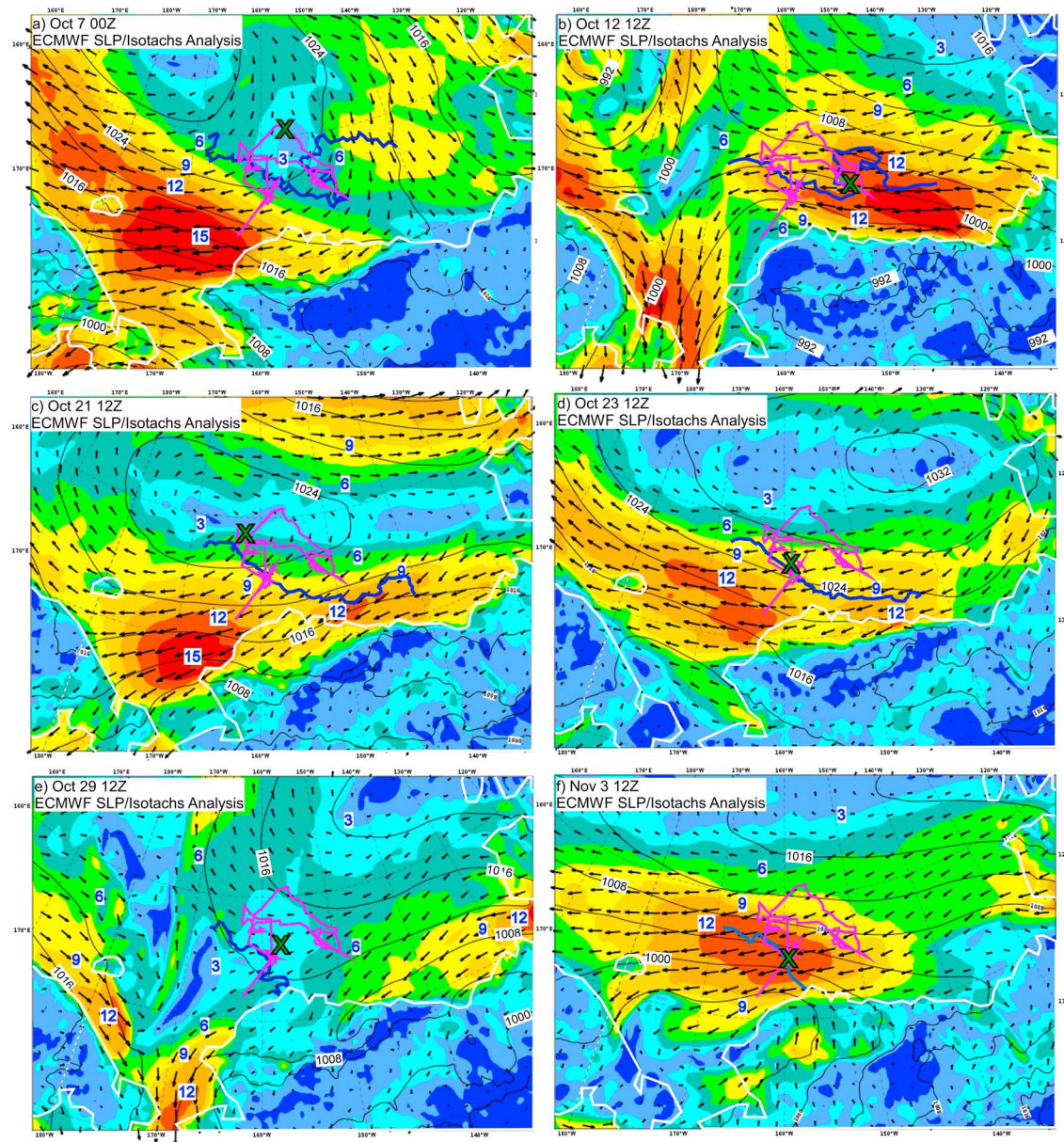


Figure 4. ECMWF operational analyses of sea level pressure (black, thin lines; mb) and near-surface isotachs (colored fields, with blue labels in m/s) for (a) 7 October 12Z, (b) 12 October 12Z, (c) 21 October 12Z, (d) 23 October 12Z, (e) 29 October 12Z, and (f) 3 November 12Z. In each panel, the ice edge near the Sea State region from AMSR2 is shown as a heavy blue line, the entire Sea State cruise track is shown as a magenta track, the track on the analysis day is shown by a neon green track, and the location of the R/V *Sikuliaq* at the analysis time is shown by a green X. The heavy white lines show the coastlines. ECMWF = European Centre for Medium-Range Weather Forecasts; SLP = sea level pressure.

that the variability shown may be due to either temporal or spatial changes. In general, because of the slower time scales in the ocean, variability in the ocean likely represents spatial variability, while variability in the atmosphere may represent either spatial or temporal changes. Reasons for a likely interpretation will be stated.

4.1. Transit 1 (T1): Initial Ice Entry, New Ice, Chukchi Shelf to Canada Basin; 4–10 October

The R/V *Sikuliaq* approached the ice edge from open water on 4 October at the beginning of the cruise, reaching the edge near 09 UTC (Figure 7a) and spent the next 21 hr quasi-stationary near the edge. At ~06 UTC 5 October, the ship transited steadily northeastward through thin-growing ice (Figure 7b) reaching an area of

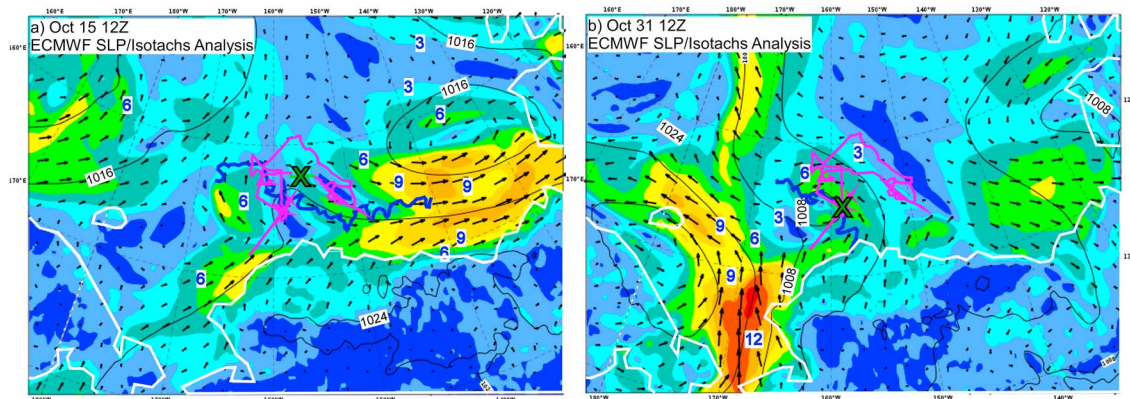


Figure 5. As for Figure 4, but showing the (a, b) two weak mesocyclones occurring during Sea State. ECMWF = European Centre for Medium-Range Weather Forecasts; SLP = sea level pressure.

existing higher ice concentration, including some MYI floes, near 12 UTC 6 October (Figure 7c). After spending nearly 48 hr at this MYI site, the ship continued the transit toward the ice edge to the SE. During this entire time, the growth of new, thin ice was extending the ice edge farther south and eastward. The transit to the SE was through thin ice of various types (see Figure 8 in Thomson et al., 2018). The ship reached the ice edge early on 10 October, spent about 8 hr over open water, and then moved back into the ice.

Figure 8 shows the near-surface environment encountered during this 2.5-day transit and includes the lowest 1,800 m of the atmospheric structure (panel a), key surface parameters (panels b and c), and the thermal structure of the upper ocean (panel d). Over the open water, the air was relatively warm ($\sim -1^{\circ}\text{C}$; red curve in panel b) and the air and ocean-surface temperatures were very near the freezing point of the seawater (blue and green curves, respectively, in panel b). Just within the ice edge (first shaded area of Figure 8),

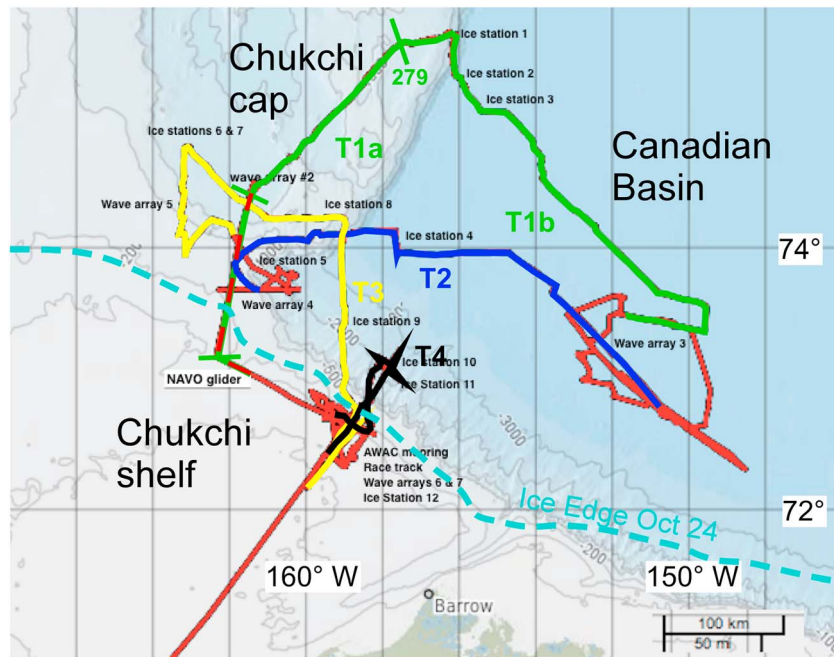


Figure 6. The Sea State cruise track showing the regional bathymetry (m) relative to the four color-coded ship transits T1, T2, T3, and T4. The two green bars on track T1a refer to the time period marked in Figure 8d, while the green bar labeled "279" shows the ship's location at 00 UTC 6 October (YD279). The dashed green shows the portion of T1a that is used as IEO in section 6. The ice edge on 24 October is a dashed cyan line.

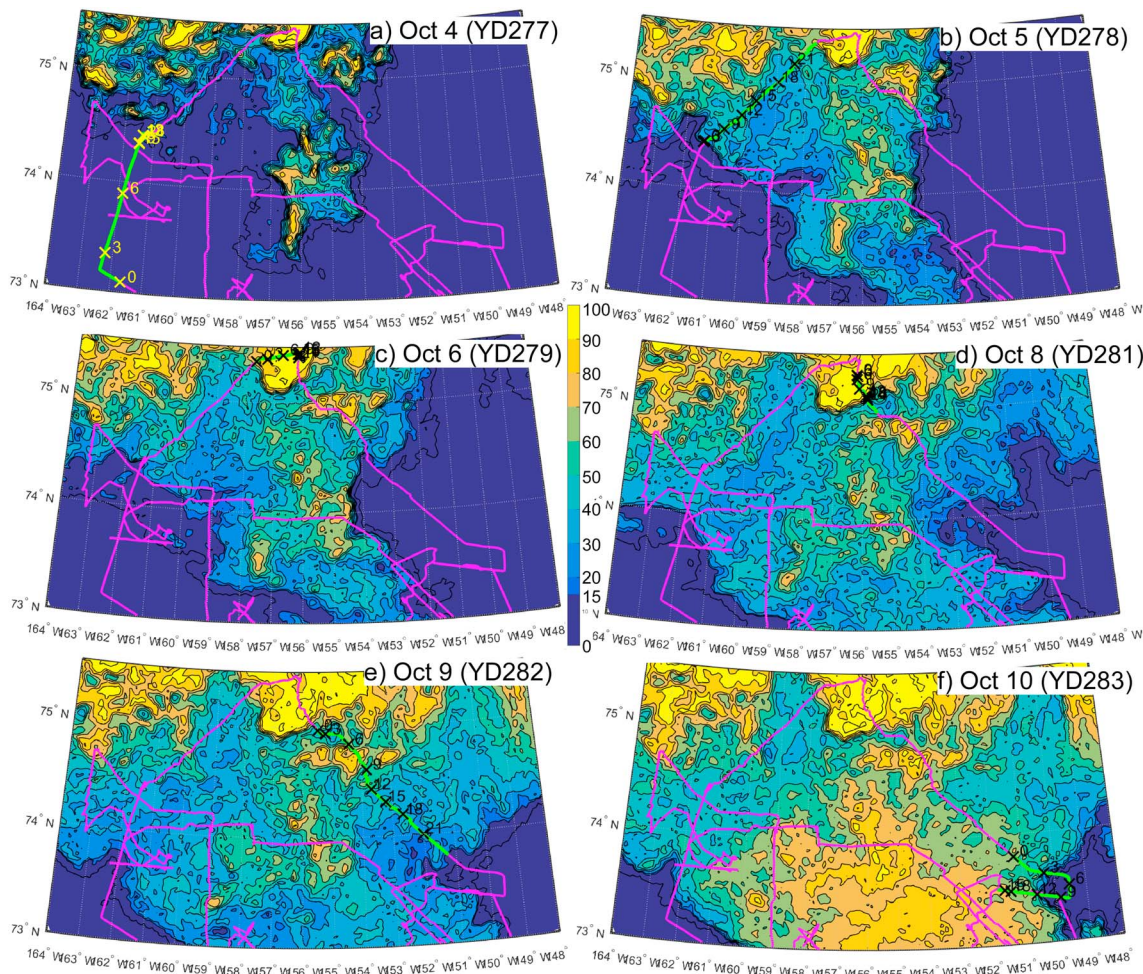


Figure 7. Sequence of daily AMSR2 ice concentrations (%) for 4–10 October. Ice concentrations >15% are shown according to the color bar. The magenta line shows the entire Sea State track of the R/V *Sikuliaq*; the neon green portion shows the track for the given day. Black labels [yellow in (a)] along green track show ship locations at 3-hr intervals (UTC). The 7 October panel is omitted as the ship was stationary.

the air temperature cooled to $\sim -3.5^{\circ}\text{C}$, while the T_{skn} of the water surface remained near the freezing point of the seawater (T_{frz}) and that of the ice surfaces was $\sim -2.5^{\circ}\text{C}$. As the ship transited further into the thin ice, the surface air temperature cooled slightly to -7°C during the night, then warmed to $\sim -4^{\circ}\text{C}$ the next day as a few hours of midday weak surface heat gain replaced the general heat loss (black curve in panel c), and then cooled to nearly -10°C . During the nearly 42 hr the ship was stationary at the ice station (second shaded area), T_a increased slightly by about 2°C . The ice concentration (A_i) was between 0% and 60% at the ice edge, but increased steadily to $\sim 95\%-100\%$ during the transit into the ice (see photo in Figure 2a). While the thickness of the few multiyear floes encountered were often 1 m or greater, the thickness of the predominant new ice was only 5–15 cm. (Note that the mean ice concentration shown is likely underestimated, as the AMSR2 values are often 20%–30% lower than those from the ASSIST and SEB techniques in this thin ice.) During the second half of this ice transit back toward the ice edge, T_a increased gradually by another 2°C but the surface (skin) temperature increased more rapidly, producing large air surface temperature differences near the ice edge. On the exit portion of this transit, the ice concentration decreased slightly to 60%–80%, before dropping rapidly right at the ice edge. The new ice continued to be quite thin (5–15 cm).

Over both the open water to the south and at the ice edge, the AMLH was generally between 600 and 1,200 m. Low clouds were present within the mixed layer, with cloud bases near 300–600 m, except for a 6-hr period over the open water where cloud bases were $\sim 1,650$ m. Despite the general heating of the lower atmosphere by the surface, the AMLH continued decreasing to only 150–350 m during the transit into the

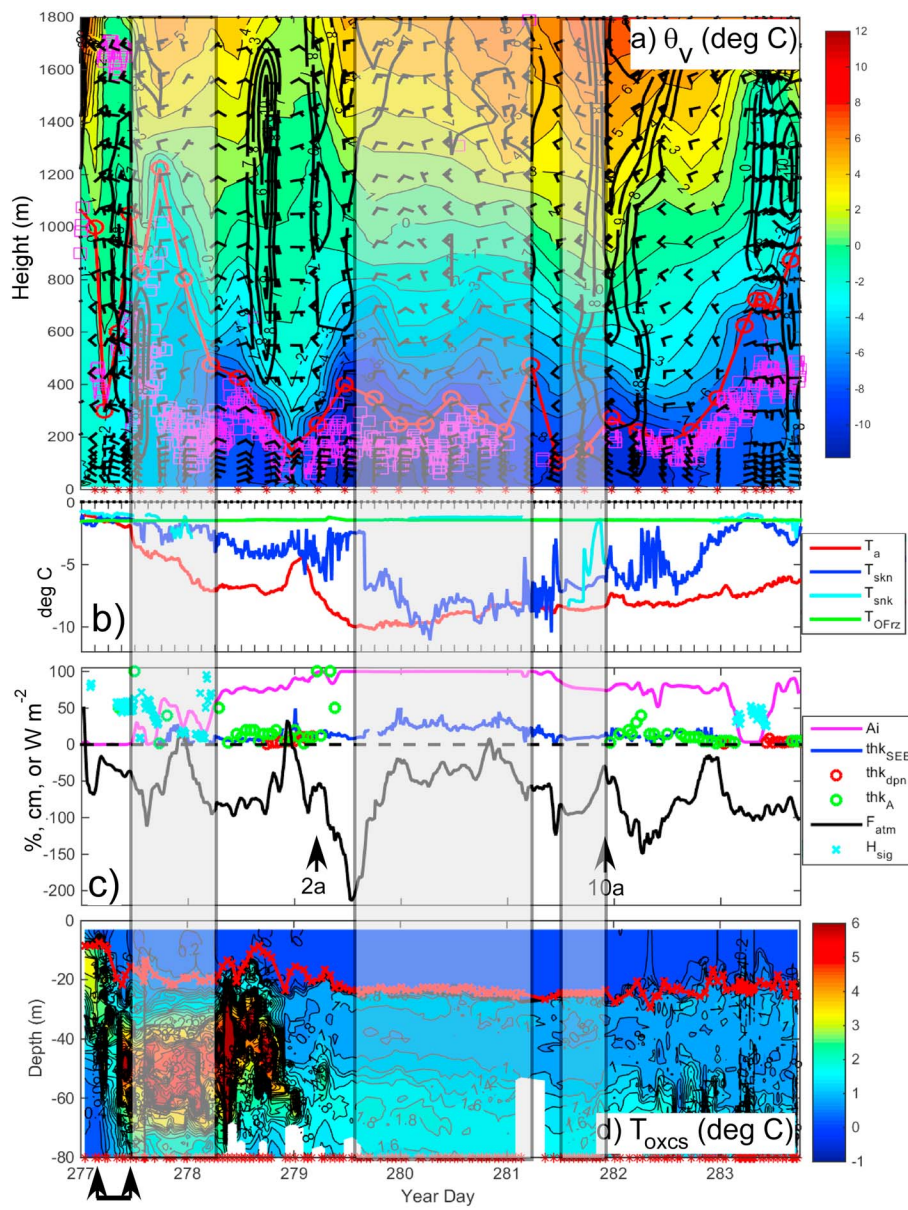


Figure 8. The air-ice-ocean environment during Transit 1 (4–10 October): (a) Time-height section of atmospheric virtual potential temperature (θ_v , $^{\circ}\text{C}$; color) and atmospheric mixed-layer height (red circles/lines) from rawinsondes. Isotachs for winds ≥ 7 m/s and wind barbs (using meteorological convention, with upward barb indicating wind from the north) are shown in heavy black. Cloud bases from the ceilometer are marked as magenta squares. (b) Air temperature (T_a), skin temperature (T_{skn}), sea snake temperature (T_{snk}), and ocean freezing point (T_{OFrz}). (c) Ice concentration (Ai; magenta line); ice thickness from SEB (blue line), ASSIST (green circles), and manual dipnet (red circles); net surface energy budget F_{atm} (black line). (d) Time-depth cross section of ocean freezing excess temperature (T_{oxcs} , $^{\circ}\text{C}$) and ocean mixed-layer depth (red “X” and line) from underway CTDs. The red “**” on the x axis in the upper and lower panels show times of the rawinsondes and CTDs, respectively. The arrows in the middle panel show times of photos in Figures 2a and 10a. The arrowed bar (bottom left) shows the time of transit from the shallow Chukchi Shelf to the deeper Chukchi Cap (marked by two green bars on track in Figure 6). The shaded regions show times when the ship was stationary or quasi-stationary.

interior of the ice, and cloud bases varied between the surface and ~ 300 m. The generally low AMLH continued throughout the entire period the ship was within the ice, only increasing near the ice edge toward the end of this transit. A continuous cloud cover was present near the ice edge at both ends of the transit, while in the interior some breaks in the clouds occurred. An atmospheric low-level jet (LLJ) at ~ 450 -m height in the along-edge northwesterly winds coincided with the low-level baroclinic zone upon

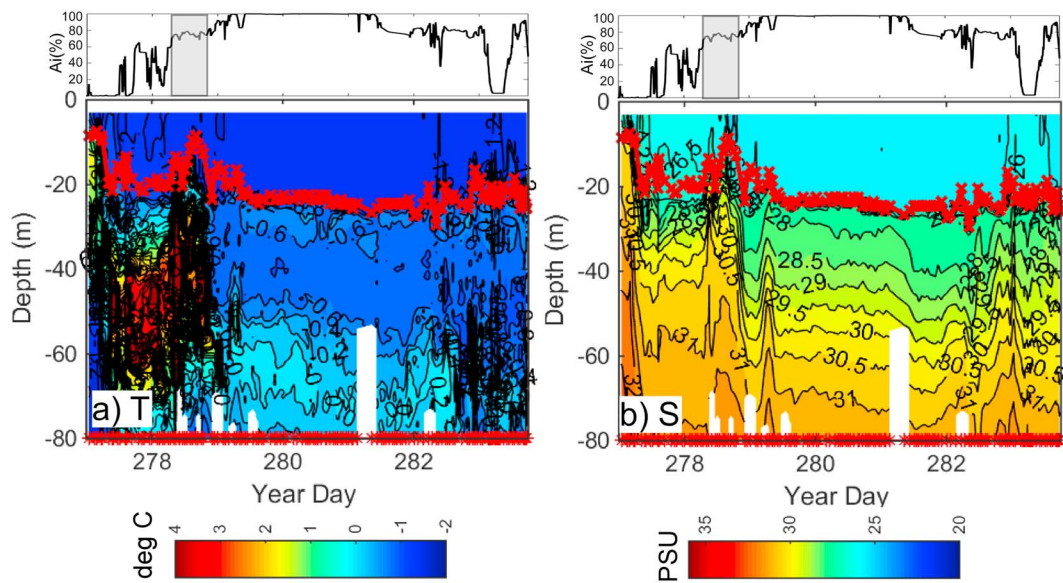


Figure 9. Upper-ocean time-depth cross sections of (a) temperature ($^{\circ}\text{C}$) and (b) salinity (S) for transit T1 (4 October through 18 UTC 6 October). The ocean mixed-layer depth (MLD) is shown (red "X" and line), while the time of each uCTD is given by the red "*" along the abscissa. The ice concentration trace is shown above each panel, and the time when crossing the region covered by ice until mid-September (Figure 3a) is shaded in the Ai box.

entry into the ice on 4 October (YD277.5 in Figure 8a). A more complex LLJ structure was present within and above the AML near the ice edge exit area on 10 October, which coincided with changing atmospheric synoptic conditions and increasing local on-ice winds.

In the open water area south of the ice on 4 October, the ocean mixed-layer depth (OMLD) was very shallow near ~ 8 m and a layer of water 3°C above the freezing point was located at ~ 16 -m depth. The surface water in the OML was a few tenths of a degree above the freezing point ($T_{\text{oxcs}} = 0.2\text{--}0.6^{\circ}\text{C}$). Coincident with a descent of the bottom bathymetry from ~ 100 m to $\sim 1,000$ m between 02 and 08 UTC 4 October (Figure 6) as the ship moved from the shallow water of the Chukchi Sea to the Chukchi Cap, the OMLD deepened to 15–22 m with water up to 6°C above the freezing point located at depths between 40 and 60 m. Near the ice edge and along the transit track, the near-surface water was close to the freezing point ($T_{\text{oxcs}} = 0.0\text{--}0.2^{\circ}\text{C}$). This $T_{\text{oxcs}} \approx 0.0^{\circ}\text{C}$ and $F_{\text{atm}} < 0 \text{ W/m}^2$ are the two requirements for ice formation, indicating that ice was forming at the ice edge and along the transit route, which is consistent with the evolution of the ice pack (Figure 7). This ice formation occurred despite the very warm water just a few tens of meters below the OMLD. This warm subsurface water is replaced by water that is only $0.6\text{--}1.0^{\circ}\text{C}$ warmer than the freezing point near 21 UTC 5 October, which coincides with the ship's arrival near the edge of the Chukchi Cap at the northernmost portion of the transit just above the bathymetric precipice dropping into the deep Canada Basin (Figure 6). Note that some pulses of slightly warmer and more saline water extend into the OML near the open water area at the end of the transit (Figures 8d and 9b), making the OML slightly shallower.

We speculate that the presence of the ice, although very thin, caused the observed lower-atmosphere cooling, lowering of the AMLH, and the low clouds within the mixed layer. These tendencies suggest that the atmospheric boundary layer is losing heat in the net despite a significant heat flux coming through the ice from the water below. Such a boundary layer heat loss may occur through turbulent mixing of heat within the AMLH from the surface to near-cloud top combined with longwave radiative heat loss from the cloud top, which is located near or just above the AMLH. The well-mixed nature of the AML ($\partial\theta_v/\partial z \approx 0$) supports this hypothesis. The AML cooling and AMLH lowering during the time the ship was quasi-stationary at the ice edge suggest that some of the atmospheric variability may have been temporal rather than spatial in nature. High pressure may have been establishing itself over the ice to the north, causing some lowering of the AMLH and outflow of colder air to the edge. The formation of ice (increase of ice concentration) during this same time (see Figure 7) may also have caused cooling and lowering of the AMLH to occur at the ice edge. These scenarios are supported by the wind shift from WNW (edge parallel) to NNE (off-ice) while the ship was

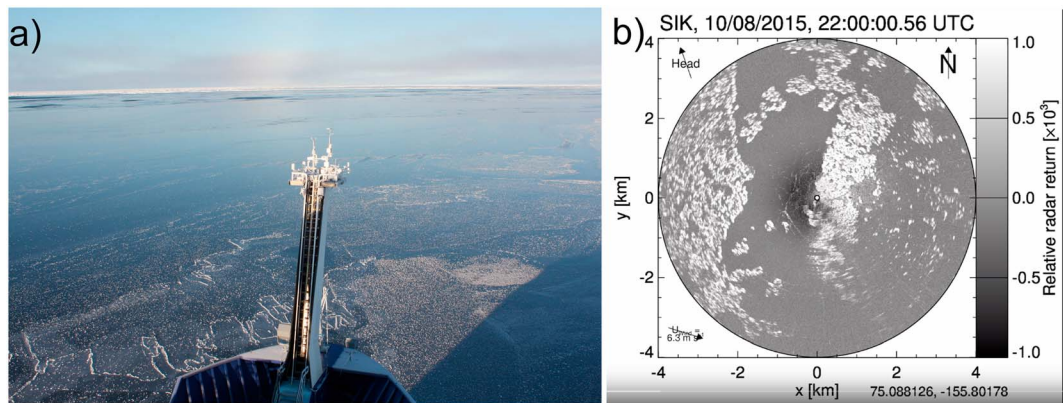


Figure 10. The upwind ice conditions representative of the period 1125–2215 UTC 8 October as shown by (a) a photograph taken at 2212 UTC 8 October and (b) a marine radar backscatter image at 2200 UTC 8 October. The ship is located at the center of (b) with the photograph taken to the left of the heading indicated in (b) by “Head” arrow.

at the ice edge (Figure 8a). The cooling over the ice produces low-level baroclinicity at the ice edge, which can cause features such as LLJs to form. The measured surface winds were ~8 m/s under the LLJ, and produced a maximum in the surface stress at ~12 UTC 4 October (Figure 11a).

To explain the observed ocean structure, we speculate that the temperature variability below the OMLD is due to sampling different water masses near this region of complex bathymetry and ocean currents combined with different ice histories, and hence surface energy fluxes. The significant transition in upper-ocean thermal structure at the beginning of the transit is likely due to water mass differences between the Chukchi Sea and the Chukchi Cap, as the changes occurred during the transit of the bathymetric slope between the two. We infer that the warm water mass at 40- to 60-m depth over the Chukchi Cap is some variant of warm Pacific Summer Water (PSW) delivered from the Chukchi Sea as either Alaskan Coastal Water (salinity ~29–32 psu) or summer Bering Sea Water (salinity ~32–33 psu) or some mixture of the two (e.g., Timmermans et al., 2014). The observed salinity of the warm water at 40- to 60-m depth (Figure 9) ranged from ~30 to 31 psu, and will generally be referred to as PSW (see also Smith et al., 2018). At the end of T1a near the edge of the Chukchi Cap and extending over the deep Canada Basin along T1b was an abruptly cooler and slightly less saline (~28–30 psu) subsurface water mass. This water mass is distinctly different from PSW and is referred to as the near-surface temperature maximum (NSTM) layer that lies just below the OML, where the NSTM is formed by summer solar heating (Jackson et al., 2010). Over the Canada Basin, some variant of PSW is present, however, but it has been subducted and modified (by mixing) and thus is cooler and lies deeper in the water column at 60- to 80-m depth (Timmermans et al., 2014). Note that an ice tongue remained over the area where we observed the much warmer water at 40- to 60-m depth as late as mid-September (Figure 3a and shading in Figure 9), perhaps inhibiting upward mixing of this heat, while open water existed much earlier than mid-September at the NE end of this transit, reinforcing this sharp transition in thermal structure. Additionally, this NE end has had several days longer of new ice cover (at least since 3 October) and is also located near the edge of the Chukchi Cap near the steep bathymetric drop-off into the Canada Basin. Hence, differences in both water masses and ice-cover history may have impacted the observed temperature profiles in the upper ocean along this initial transit into the new, thin ice.

Other air-ice interaction processes captured and quantified during transit T1 include ice-type-dependent air-ice turbulent flux relationships, changes in the relative importance of the turbulent heat fluxes and the long-wave radiative heat loss from the surface between the ice edge and the ice interior, and the relationship between ice drift and the wind. Excellent turbulent flux measurements were obtained over an extensive area of 7- to 12-cm-thick nilas ice upwind of the ship while it was stationary between 1125 and 2215 UTC 8 October (Figure 10). The covariance stress was clearly smaller than the stress obtained from the inertial dissipation (ID) or bulk techniques (Figure 11a), which were very similar. The smaller covariance stress, which is the best estimate of the true stress with the least assumptions, is likely due to the very smooth *glass-like* nature of the ice surface. Note the lack of marine radar backscatter from the smooth nilas ice (Figure 10b), while the MYI at a distance of 2 km or more shows a stronger backscatter. However, during other times of transit T1,

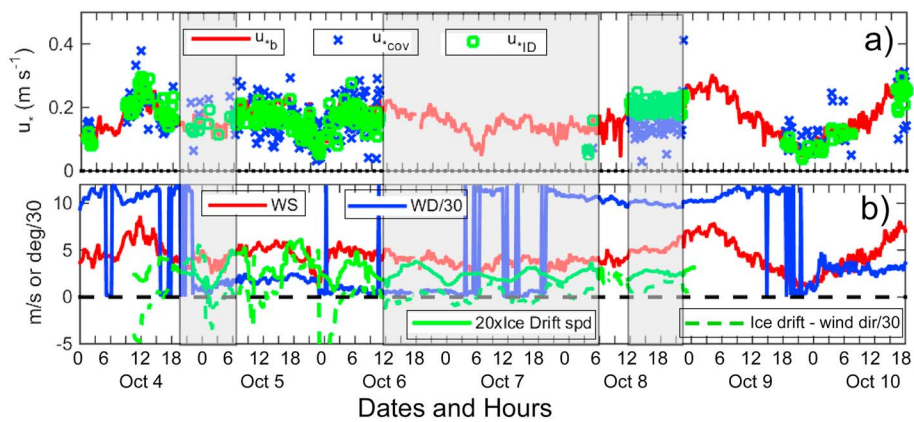


Figure 11. Transit T1 time series of (a) friction velocity (u^*) from bulk scheme (red line) and covariance (x) and inertial dissipation (square) calculations, and (b) wind speed (red), wind direction (blue), ice drift speed (solid green), and ice drift direction minus wind direction (dashed green). The times when the ship was stationary are shaded.

such as on 4–6 and 9 October, when the thin ice had a slightly rougher surface (rafted nilas, with some pancakes or small MYI floes; e.g., Figure 2a), the covariance stress tended to be close to or slightly greater than the bulk and ID stress, while the ID stress was a little less than the bulk stress. The covariance stress showed the greatest scatter.

The sea ice drift direction and speed were obtained from the marine radar images as described in section 2 (e.g., Lund et al., 2017). The average drift of the sea ice tended to be at $\sim 3.3\%$ of the wind speed and $\sim 18^\circ$ to the right of the wind direction ($\text{dir}_{\text{ice}} - \text{WD} > 0$; Figure 11b), though the time series shows a clear tendency for an inertial oscillation in both speed and direction, especially during the first half of the transit. While there are no inertial oscillations in the wind, ice motions show modulations in both speed and direction with a period of 12 hr. The amplitudes of the speed and direction oscillations decreased noticeably near 06 UTC 6 October. The larger inertial amplitudes occur in water over the Chukchi Cap, with significant periods of time when the ice drift is strongly to the left of the wind. In the water over the deep Canada Basin, the ice drift is nearly always to the right of the wind. This change suggests that ocean currents near the shelf break may significantly affect the ice drift, while the wind is dominant over the Canada Basin.

Figure 12 shows that all terms of the surface energy budget contribute to surface heat loss through the entire transit except the net shortwave radiation. LW_n is at times only weakly negative, while during clear periods it

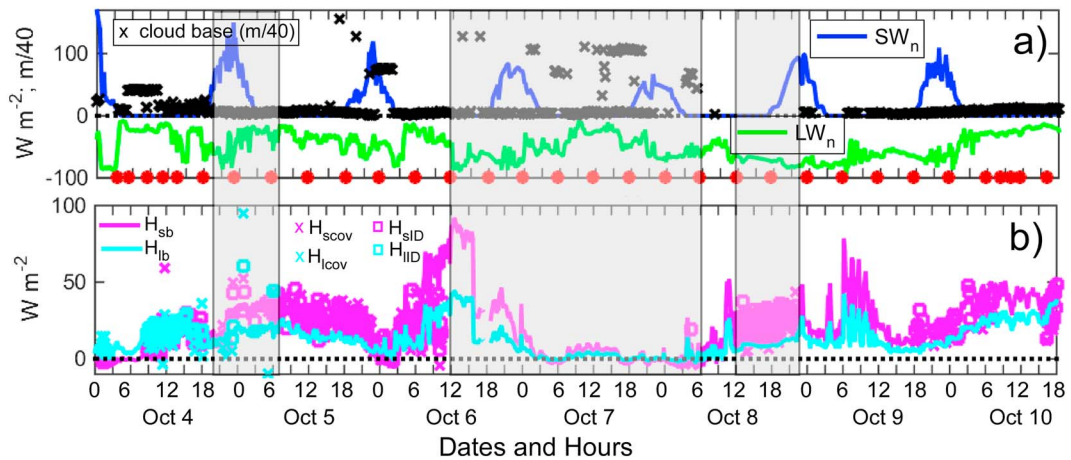


Figure 12. Ten-minute time series of terms of the surface energy budget during transit T1, showing (a) net shortwave radiation (SW_n), net longwave radiation (LW_n), and cloud base, and (b) sensible (H_s ; magenta) and latent (H_l ; cyan) heat flux. Panel (b) shows the bulk (solid), covariance (x), and inertial dissipation (square) values. The red dots in (a) show times of soundings.

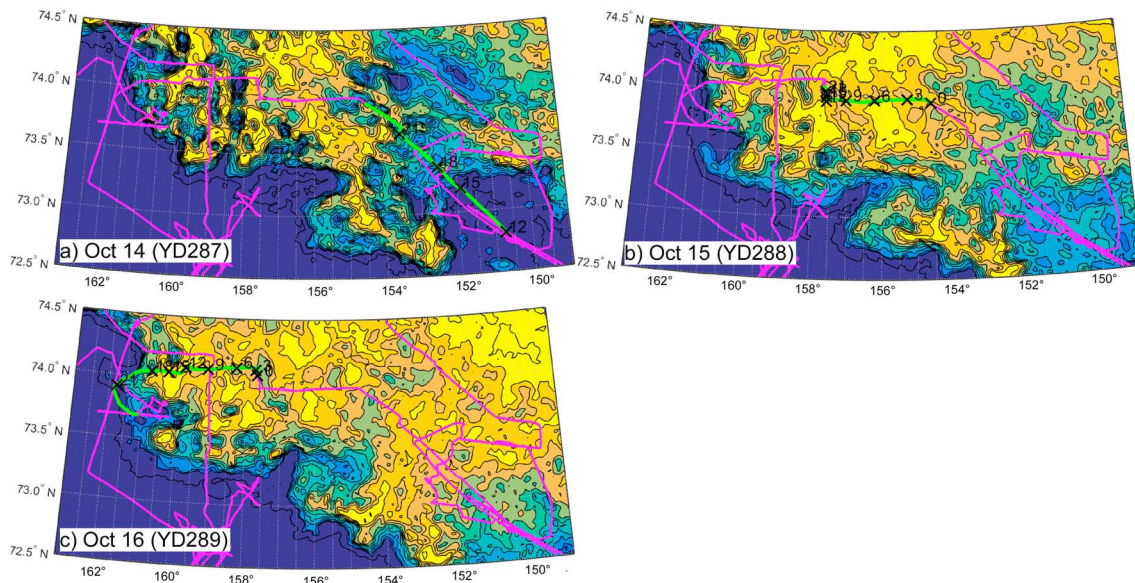


Figure 13. As for Figure 7, but for transit T2 on 14–16 October (YD287–289).

is strongly negative. Despite the warmer ice surface temperatures near the ice edges, which would enhance the outgoing longwave radiation and decrease LW_n , LW_n is less negative near the ice edge because of the enhanced downwelling LW radiation from the clouds. While the turbulent heat fluxes are both positive (cooling the surface) through the entire transit, the sensible heat loss is greater than the latent heat loss throughout. Near the ice edge, $H_s + H_l$ is generally greater than LW_n . The bulk turbulent heat fluxes are in reasonable agreement with the mean covariance and ID heat fluxes, though covariance and ID latent heat fluxes are only available during the first ~24 hr of the transit due to riming of the Licor sensor.

Transit 1 demonstrated many of the atmospheric, ice, and ocean features and interactions that will be seen in some of the subsequent transits and ice edge areas.

4.2. Transit 2 (T2): Trans-Ice, Canada Basin; 14–17 October

Transit T2 began immediately after the strong wind event sampled at the ice edge on 11–14 October (see Smith et al., 2018) and 4 days after transit T1 ended. It had a duration of 3 days as the R/V *Sikuliaq* transited the new, growing ice pack from east to west (Figure 13), ending in open water late on 16 October (YD289). During the transit, the ice edge expanded slightly southward and the ice concentrations increased within the existing ice, becoming spatially more homogeneous near 70%–100%. Transit T2 occurred from within the deep Canada Basin to the shallower water over the bathymetric slope from the Chukchi Sea to the Chukchi Cap sampled on 4 October (YD277) at the beginning of transit T1 (see Figure 6). The first half of the transit was primarily through rafted and/or compacted pancake ice, while other ice types, including some small MYI floes, were also seen during the second part of the transit (see Figure 8 of Thomson et al., 2018).

The transit occurred under a weak high-pressure area located between three weak low-pressure centers (Figure 5a). This resulted in weak-to-moderate WNW winds as the first low exited the area to the east, followed by winds that backed to the SE as the second low passed to the ship's south, followed by a shift back to weak-to-moderate W winds as the ship exited the ice at the end of the transit. The coldest air temperatures on this transit were only -6°C in the WNW airflow behind the first low-pressure system (Figure 14b) and remained within -5 to -3°C through the remainder of the ice interior. T_a was $\sim -2^{\circ}\text{C}$ near both ends of the transit. The ice thickness estimates varied significantly between the techniques during the first part of the transit, ranging between 5 and 30 cm (Figure 14c). During the second part of the transit, the techniques were more consistent, with thickness estimates between 8 and 20 cm. The surface temperature of this thin ice was warmer than the local T_a through almost the entire transit. This ice surface was losing heat to the atmosphere through the entire transit, averaging -51 W/m^2 , with the greatest loss of more than -100 W/m^2 occurring early on 15 October (YD288) with the deepest cold air in the WNW airflow behind the first

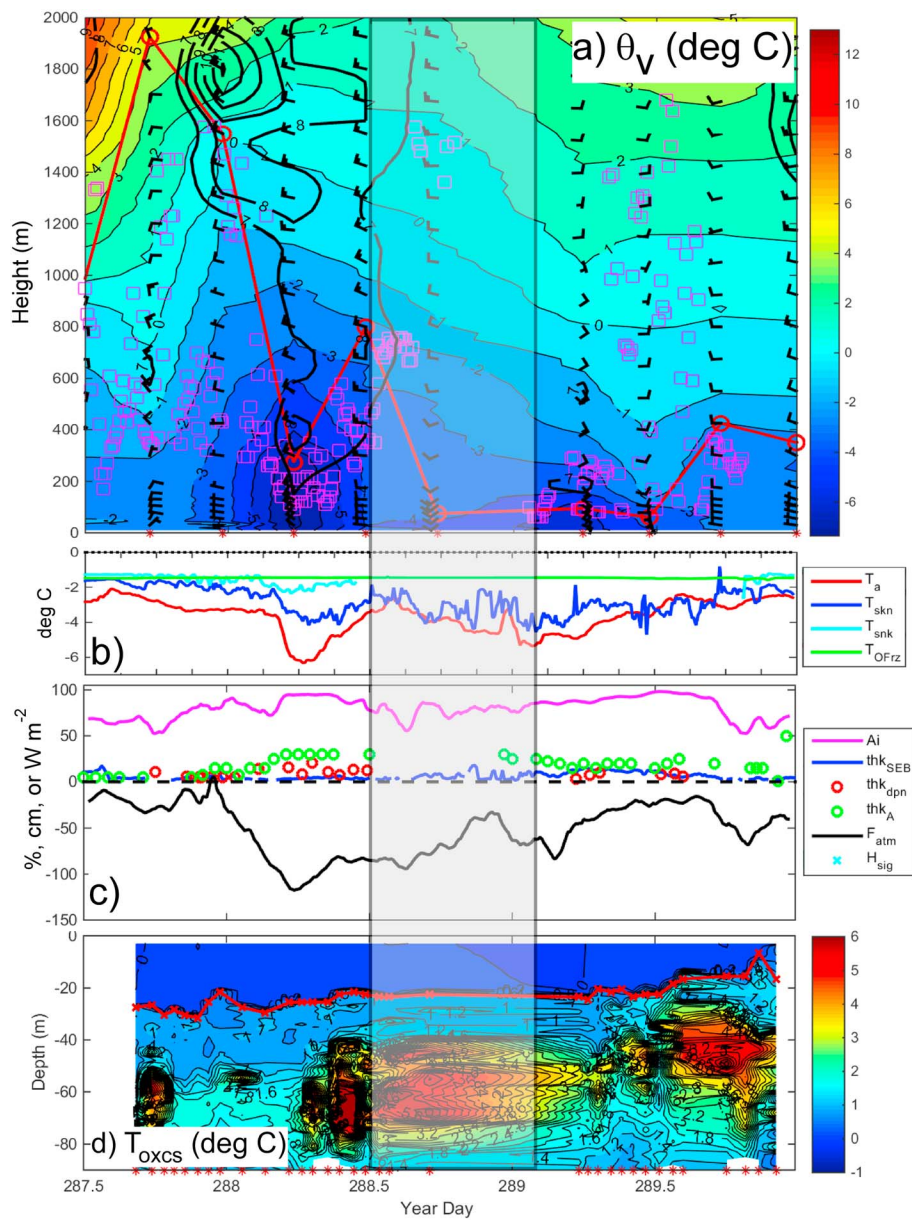


Figure 14. As for Figure 8, but for transit T2 on 14–16 October (YD287–289).

low-pressure system (Figure 14a). After this initial cold air, the lower atmosphere warmed steadily through the entire transit. As for transit T1, the AML was deepest over the open water areas near the ice edge and quite shallow over the ice interior despite the unstable surface layer ($T_a < T_{\text{skn}}$) and the net surface heat loss to the atmosphere ($F_{\text{atm}} < 0 \text{ W/m}^2$). Most of the surface heat loss was through longwave radiation, though turbulent sensible and latent heat fluxes also contributed to the loss (not shown), despite a few periods of weak sensible heat gain by the surface. While low clouds were present through most of the first half of the transit, only sporadic low clouds occurred during the second half, some over the ice and some at the ice edge (Figure 14a). No obvious LLJs existed at the two ice edges of this transit.

The OMLD decreased steadily through the entire transit, starting at ~30-m depth and ending at ~8–18 m near the western ice edge above the sloping bathymetry (Figure 14d). This shallow OMLD at the end of transit T2 is in agreement with the OMLD measured at the same location at the beginning of transit T1. The temperature in the OML was consistently very near the freezing point until the open water patches at the end of the transit, consistent with the high and increasing ice concentration along the entire track. While patches of very

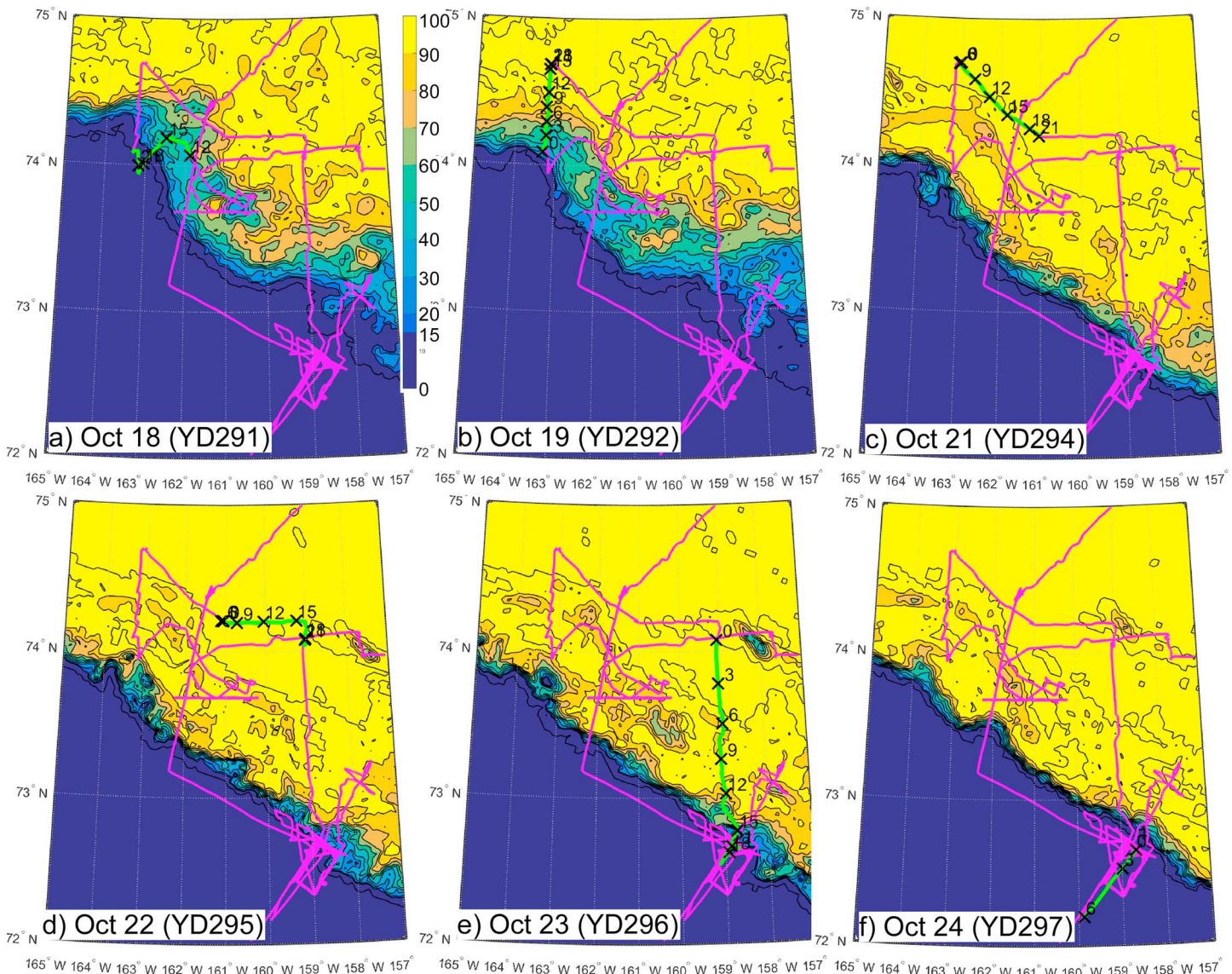


Figure 15. As for Figure 7, but for transit T3 on 18–24 October (YD291–297).

warm water occurred at 50- to 70-m depth at the beginning of the transit, this warm water became more extensive and moved upward in the water column to depths of 30–60 m as the ship approached the bathymetric slope along the Chukchi Cap. Again, this is consistent with the earlier observations at this same location.

The radar-determined ice drift was both to the right and left of the observed wind direction, with much more of the transit showing ice drift to the left of the wind than for transit T1 (not shown). The variability in ice drift speed and direction was not as clearly linked to the inertial cycle as for transit T1.

4.3. Transit 3 (T3): Ice Edge Atmospheric LLJs, Shelf-Cap-Basin Corner; 18–24 October

Ice transit T3 begins with an initial 18-hr transit into the ice sampling energy fluxes in a moderate off-ice wind, followed by a series of ice stations in high-concentration new ice (Figure 15). The exit from the ice on 23 October also occurs with a direct 18-hr ship transit from the ice interior to the open water at the ice edge, with the farthest off-ice (open water) transit of Sea State occurring early on 24 October. During 18–24 October, the ice edge only moved slightly southward, but the ice concentration increased in low-concentration areas along the edge and embayments along the edge filled in, making the ice edge more

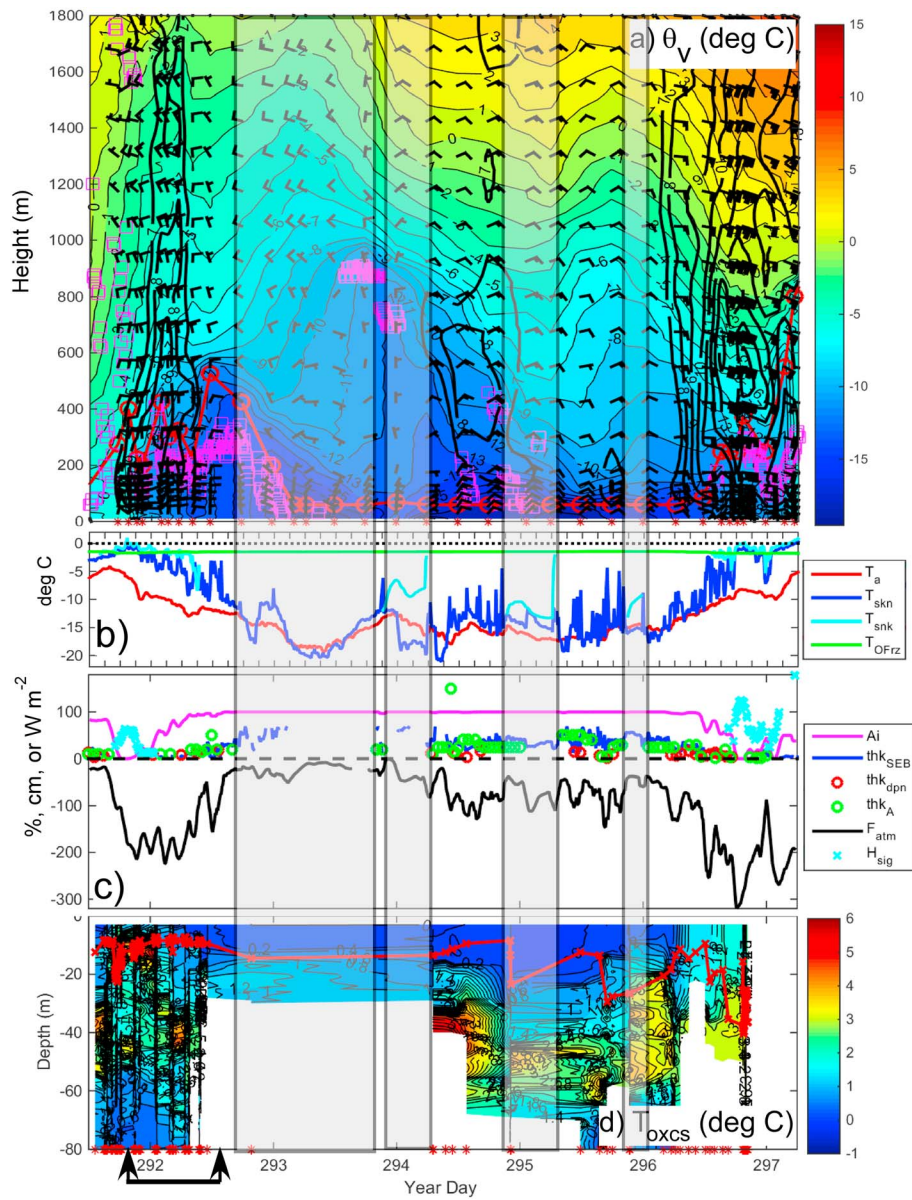


Figure 16. As for Figure 8, but for transit T3 on 18–24 October (YD291–297). The shaded areas show times when the ship was stationary, while the arrowed bar indicates a 17-hr time period when six 1-hr-long stationary flux stations were done during the initial transit into the ice.

linear. It is noteworthy that this linear ice edge is parallel to and coincident with the steep bathymetric slope that lies between the shallow Chukchi Sea and the deep Canada Basin (see Figure 6). This observation suggests that processes, likely mostly ocean processes, exist along this slope that tend to slow the southward ice advance, and producing an apparent *loitering* of the advancing autumn ice edge, as noted for summer-retreating ice edges (Steele & Ermold, 2015).

The off-ice airflow sampled during the initial entry into the ice on transit T3 had a temperature of -10° to -5°C and was much colder than the surface temperature, which was at or just below the seawater freezing point (Figure 16b). This cold air temperature was due to the much colder air (-20° to -13°C) subsequently encountered over the interior of the new ice just to the north. T_a remained in this range through the entire transit until exiting over the open water on 23 October, when T_a again warmed to -10° to -5°C . The ice concentration was near 100% in the ice interior, the ice thickness was typically 20–50 cm throughout the transit (Figure 16c), and the surface skin temperature was frequently near the air temperature of the ice interior. This

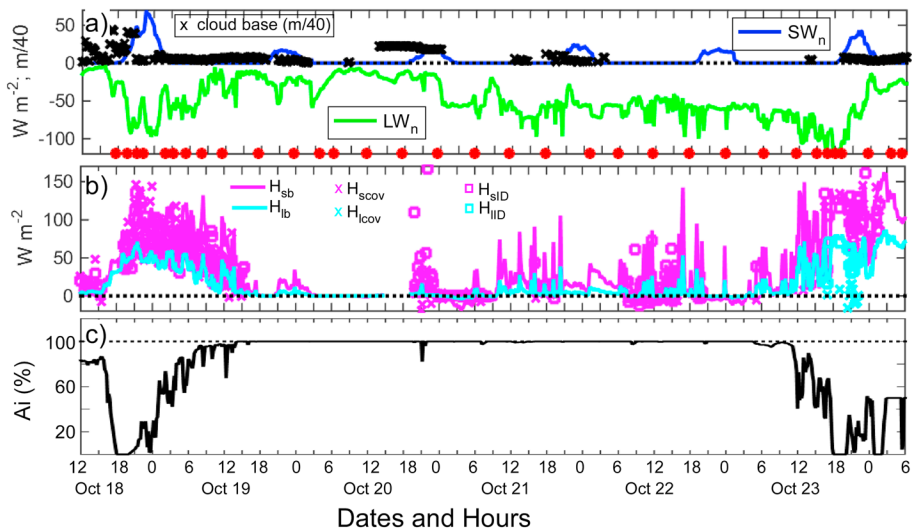


Figure 17. As for Figure 12, but for transit T3 October 18–24 (YD291–297). Panel (c) shows the ice concentration A_i (%).

transit showed the first significant snow cover on the new ice, with up to 10 cm noted on 19 October near the northern end of the initial on-ice transit. Areas of 1–5 cm of snow on the ice were also noted later during the transit. This snow cover may have been produced by a mesolow and associated cloud band seen to the east of the ship on satellite images at 2219 UTC 18 October (not shown) at the onset of transit T3, and which deposited snow on the ship's radiometers shortly before 16 UTC 18 October. Figure 2b illustrates the interior ice environment during this transit. Over thinner ice or leads, T_{skn} was substantially warmer than T_a , while during other periods T_{skn} cooled below T_a .

While the ice interior surface lost energy to the atmosphere at a modest rate of -100 to -20 W/m^2 , very rapid heat losses of 200 – 300 W/m^2 occurred in the broken ice cover and open water near the ice edge at both ends of the transit (Figure 16c). The heat loss from the interior was primarily due to longwave heat loss ($LW_n \sim -60$ to -20 W/m^2), though the turbulent heat losses contributed $\sim -20 \text{ W/m}^2$ (Figure 17). The longwave heat loss at the ice edge was slightly greater than that in the interior ($\sim -80 \text{ W/m}^2$), but the heat loss from the turbulent fluxes was 2–3 times that amount. This large turbulent heat loss at the ice edge is due to a combination of the large air-sea temperature differences because of the off-ice winds and the strong winds (LLJs) at the ice edge. While not evident in Figure 17 because of the coarse temporal resolution, the bulk-sensible heat fluxes between 18 UTC 18 October and 15 UTC 19 October were significantly larger than the covariance and ID heat fluxes. This is likely due either to an underestimation of the ice concentration or to poor T_{skn} sampling by the radiometers as the ship was frequently stationary. The bulk u_* is also slightly greater than the covariance and ID u_* values for the same reason (not shown).

While a LLJ was seen in the lower troposphere at each end of transit T3, their characteristics differ. The one seen on 19 October had characteristics of a density current, with the northerly wind directly from the ice and the LLJ core of 10 m/s was within the AML at ~ 200 – 300 m height. The LLJ at the ice edge on 23 October was primarily along-ice with only a small off-ice component, with the LLJ core of 15 m/s located above the AML at 500–700 m. This latter one was likely produced through thermal wind effects, as discussed by Guest et al. (2018). As was seen for the other transits, the AMLH was higher near the ice edge and over the open water than over the interior of the ice, where it was very shallow (below 100 m). Low-level clouds were primarily only observed near the ice edges of this transit. The significant wave heights (H_{sig}) in the moderate off-ice winds on 19 October were only about 75 cm due to the very short overwater fetch of the winds, while H_{sig} near the ice edge on 23 October was up to 2 m within ~ 50 km of the ice edge (Figure 16c). Note, however, that the winds actually had a fetch of ~ 100 – 150 km because of their oblique off-ice direction. The marine radar showed that the wave directions were about 50° to the right of the wind (i.e., from 140° rather than 90°), giving the waves an even greater fetch.

Figure 16d shows that the OMLD is very shallow (~ 10 m) at the ice entry point and underneath the continuous ice cover at the western end of this transit. During the transit into the ice on 19 October, small-scale

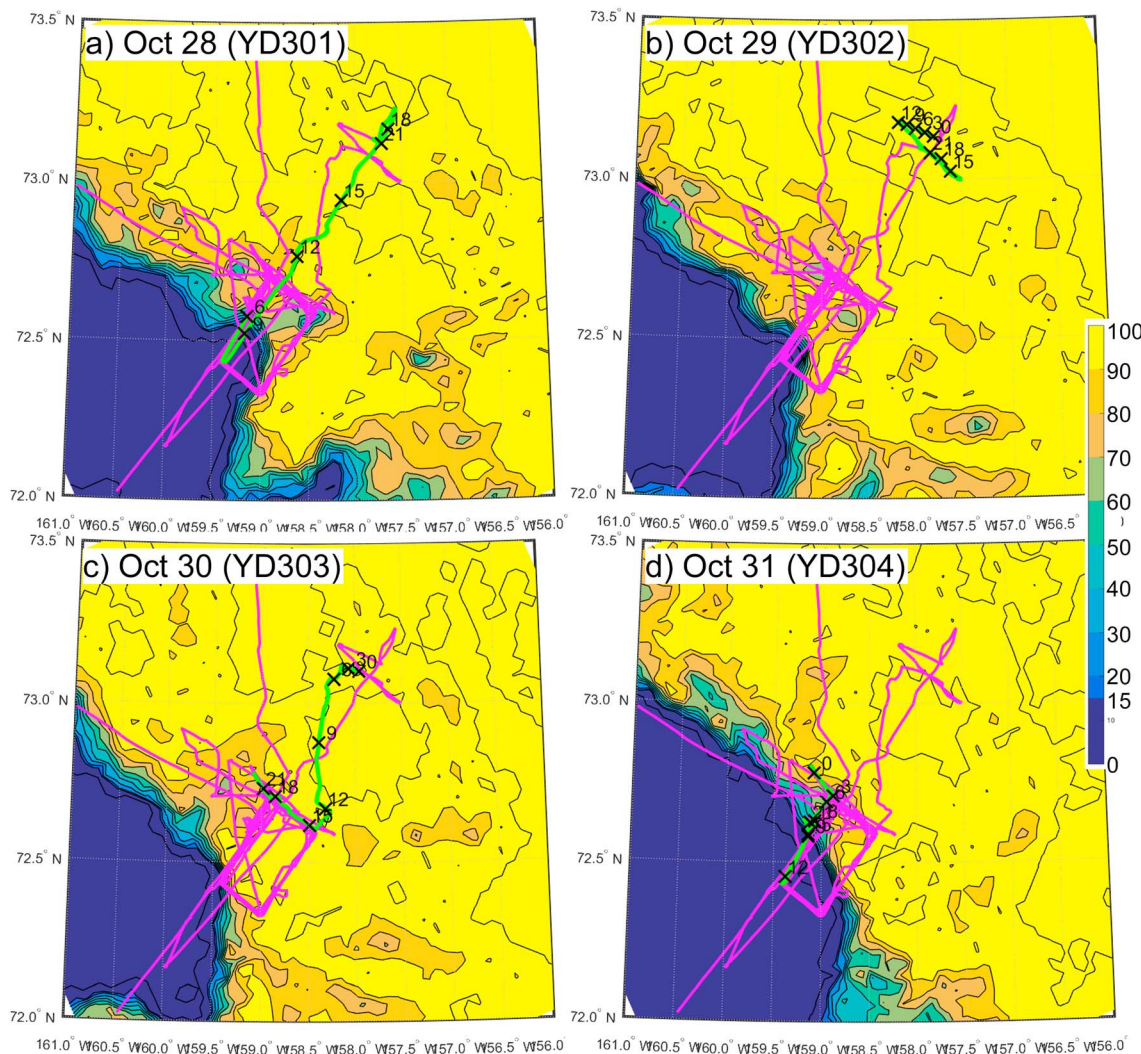


Figure 18. As for Figure 7, but for transit T4 on 28–31 October (YD301–304).

variability of the water temperature below the OML is seen in the area of rapidly cooling water and ice formation. This is occurring over the bathymetric slope from the Chukchi Shelf to the Chukchi Cap (Figure 6). Near 16 UTC 21 October (YD294.7), transit T3 crosses the same area sampled in transit T1 (it was at the ice edge then, Figure 15c). The very warm water seen at 40–60 m depth then is now seen at 35–50 m depth 17 days later (compare Figures 8d and 16d). The water sampled between 18 and 24 UTC 22 October (YD295) was also sampled at 09 UTC 16 October (YD289) on transit T2. The OMLD of ~25 m on transit T3 is about the same as seen on transit T2, while the warmer water near 40-m depth is also present in both samples. Hence, these uCTDs suggest that the upper-ocean thermal features vary primarily spatially while few changes occur over the 1- to 2-week time scales of this cruise. At the 23 October ice edge, the OMLD varies greatly spatially between 10 and 40 m and the ocean temperatures very close to the ice edge are 1–2°C above its freezing point. These warm ocean temperatures are the likely reason why the ice edge has not yet progressed south from this point.

4.4. Transit 4 (T4): Ice Entry and Exit; Thicker Ice; Coldest Temperatures; Shelf Break; 28–31 October

Ice transit T4 occurred on 28–31 October (YD301–304) as the ship left the slowly advancing ice edge and penetrated ~100 km into the new ice, where a few short ice stations were performed during the course of few days before the ship returned again to the same ice edge area from which it started (Figure 18). This relatively short transit goes from shallow water (~60-m depth) over the Chukchi Shelf to much deeper water

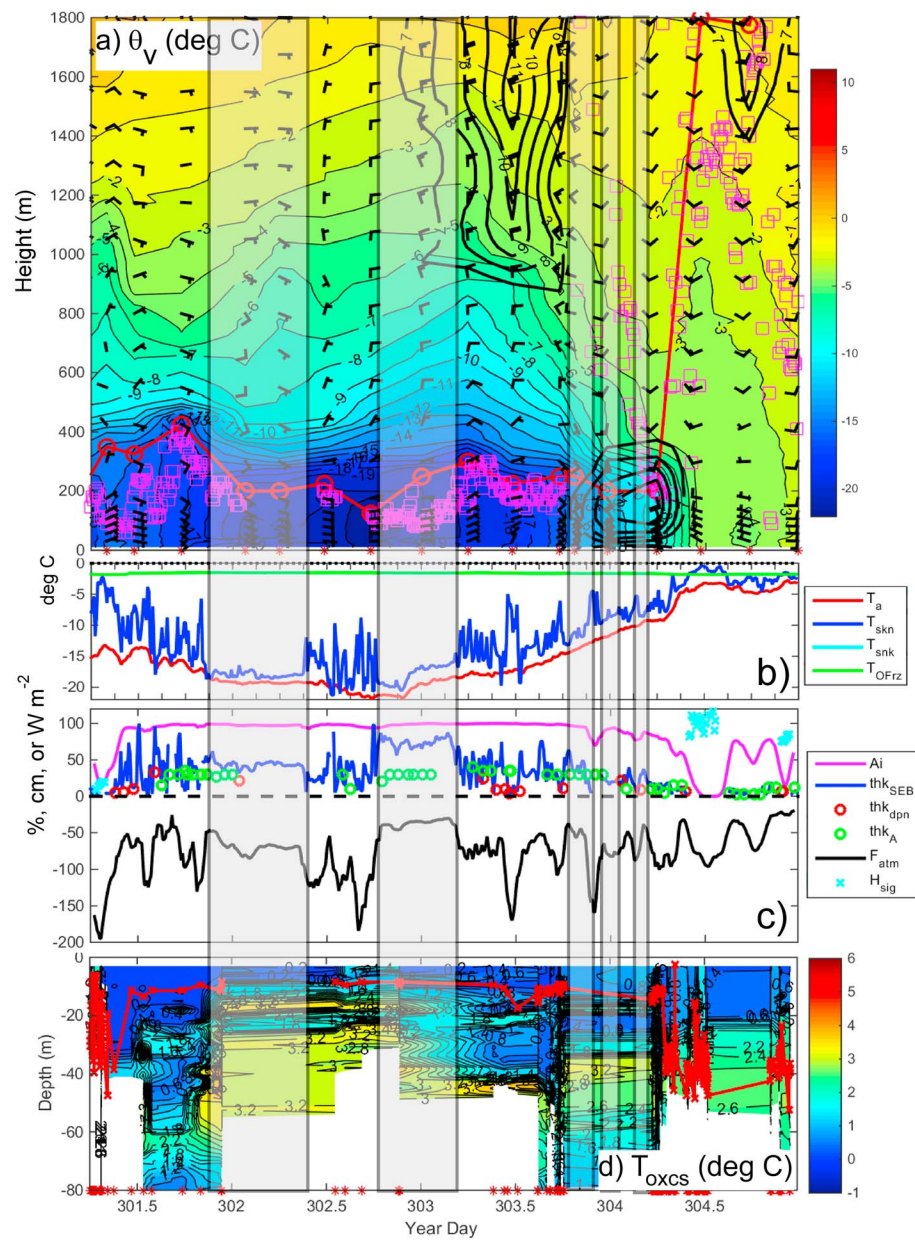


Figure 19. As for Figure 8, but for transit T4 28–31 October (YD301–304).

(2,500 m) at the edge of the Canada Basin. AMSR2 shows very little change in ice concentration in the ice interior during this time, though the ice edge advanced slowly toward the SW for the first 3 days and then retreated on the last day (31 October).

The T_a at the ice edge was already quite cold at the beginning of the transit (-15 to -13°C), but the air over the ice interior was even colder (-22°C ; Figure 19b). T_{skn} was up to 10°C warmer than T_a both at the ice edge and in the ice interior, particularly over the numerous leads and thin ice areas. The ice concentration in the interior was 95%–100%, though it decreased somewhat near the ice edge, especially upon exiting. Note that the ship spent significant time near the ice edge on 31 October, including exiting and reentering the ice, before finally exiting (Figures 18d and 19c). The ice thickness was generally 30–40 cm, but thinner near the ice edge (10–20 cm). However, the thickness from the KT15 radiometers (thk_{SEB}) showed significant spatial variability as the ship was moving, especially during the first 12 hr after entering the ice where thicknesses varied between 5 cm and 1 m. A thin (2–5 cm) snow cover was present, which artificially increases thk_{SEB} .

by 15–35 cm, possibly accounting for some of the thickest values. The thinner ice corresponds to warmer surface temperatures and greater surface heat loss (Figures 19b and 19c). The heat loss in the ice interior was approximately equally distributed between the longwave radiation and the sensible heat flux (not shown). The latent heat flux was only of importance at the ice edges. In the ice interior, ice drift was nearly always to the right of the wind, though near the ice edge the relative drift direction was much more variable, with significant periods when the ice drifted to the left of the wind. Waves were very small ($H_{\text{sig}} \sim 25$ cm) in the open water at the onset of the transit, but larger ($H_{\text{sig}} \sim 1.0\text{--}1.2$ m) upon exiting the ice.

The AMLH was only 300–400 m at the ice edge at the onset of the transit, but decreased to 200–300 m over the ice interior. As the ship exited the ice at the end of the transit, the AMLH soared to 1,800 m, one of the largest values seen on the entire cruise, coinciding with warm T_a . The high AMLH and T_a are likely due to the presence of unstable air in the warm sector of the approaching mesoscale low-pressure system (Figure 5b). As the ship made some maneuvers near but within the ice edge near 00 UTC 31 October, it encountered a distinct LLJ with winds from the SE and S associated with the strong, low-level baroclinic zone at the ice edge. The soundings suggest that this LLJ was centered near the top of the shallow AML before it deepened. It is unclear what role, if any, the approaching mesoscale low pressure system had in the formation of this LLJ. It was cloudy for much of this transit, with the exception of a number of hours on 29 October. Over the ice interior, the cloud bases were low, 50–150 m below the AMLH. However, near the ice edge at the end of the transit, the cloud bases were substantially higher (600–1,800 m) both above the LLJ and at the time of the deep AMLH.

The OMID is very shallow under the ice (10 m), while in the open water areas near the ice edge it is substantially deeper but very variable (15–45 m; Figure 19d). In the ice interior, water that is 1–2°C above the freezing point exists very near the bottom of the ice, often at 10–12 m but sometimes 3–5 m. The vertical thermal structure of the upper ocean is very complex, both under the ice in the interior and near the ice edge. Significant variability occurs over short distances, so the temporal display of the uCTDs in Figure 19d does not represent this variability well.

5. Lower-Atmosphere and Upper-Ocean Conditions at the Ice Edge

During Sea State, the R/V *Sikuliaq* conducted the four ice transits described above as well as four periods making measurements near the ice edge. The locations of these ice edge studies relative to the bathymetry are shown by the red ship tracks in Figure 6. This section will summarize these ice edge sampling periods, focusing on the two that were done at the same location near the Chukchi Shelf break where measurements were repeatedly made around a rectangular course referred to as the *racetrack*. The racetrack provides Eulerian measurements of the evolution of the conditions at this ice edge location. A fifth ice edge period, later to be referred to as IE0, occurred at the beginning of transit T1a and was briefly discussed in section 4.1.

5.1. IE1 (WA3; 11–14 October)

The first ice edge period (IE1) was conducted over the Canada Basin at the time of a strong on-ice wind event between transits T1 and T2. This period is also referred to as *Wave Array 3* (WA3). Various aspects of the environmental conditions, including the atmospheric LLJ and interactions between the atmosphere, waves, ice, and upper-ocean thermal structure and evolution are discussed by Smith et al. (2018) and Guest et al. (2018), so will not be repeated here. The upper-ocean structure during IE1 is well represented by the structure seen at the end of transit T1 (Figure 8d) and the beginning of transit T2 (Figure 14d).

5.2. IE2 (WA4; 16–18 October)

This ice edge period occurred on the western side of the area of new ice transited by T2. During this period, the ice was generally thin, though with much greater concentration than suggested by AMSR2. Hence, the open water areas were quite small. T_a was near -3°C over the open water and very thin ice (2–5 cm) and dropped to -6°C over the slightly thicker ice (10–20 cm) during the latter half of the period. T_{skn} was 1–2°C below the freezing point except for the small area of open water where it was at the freezing point. The AMLH was ~ 400 m over the thin ice, ~ 900 m over the open water, and $\sim 150\text{--}300$ m over the slightly thicker ice. The thicker ice was associated with a marked low-level cold pool in the atmosphere of ~ 500 m depth. Winds were very weak (<5 m/s) and no LLJs were seen. Values of $F_{\text{atm}} \approx -80$ to -50 W/m 2 were found over the very thin ice and open water, while values of $F_{\text{atm}} \approx -50$ to -20 W/m 2 were found over the thicker

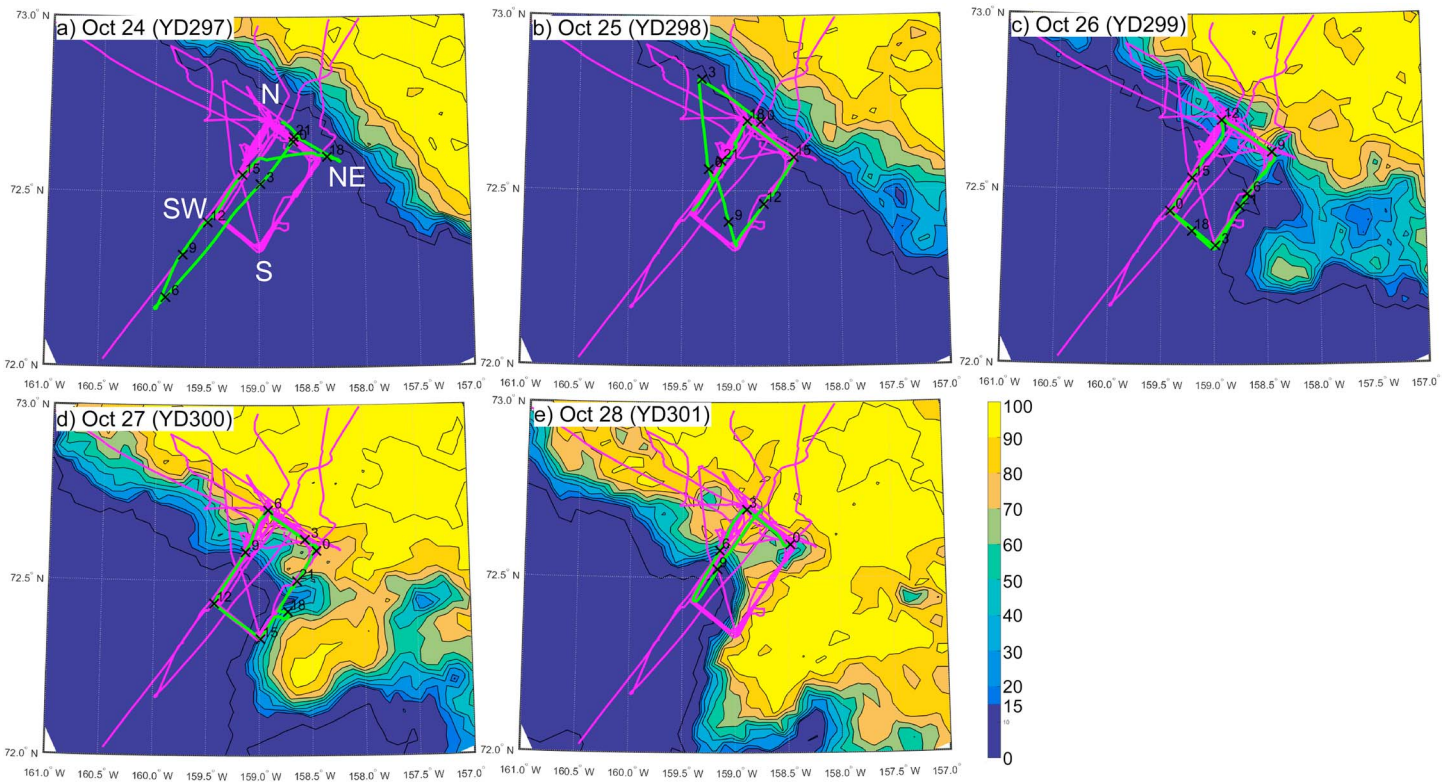


Figure 20. As for Figure 7, but for ice edge period IE3 (RT1) on 24–28 October (YD297–301). The racetrack corners referred to in the text are labeled in (a).

ice. Ice drift speed and direction varied substantially, with direction being up to 90° both to the right and left of the wind. The OMLD was shallow but variable, ranging between 7 and 28 m, with small-scale variability. The OML T_{oxcs} was generally 0.0 – 0.2°C , except near the open water area where $T_{\text{oxcs}} \approx 1.0$ to 2.5°C both in the open water and under nearby ice. Throughout the IE2 area, patches of $T_{\text{oxcs}} > 3.0^\circ\text{C}$ were found below the OMLD.

These are the main features observed during IE2, and do not provide unique environmental characterization that warrants further discussion in this study. Additional observations of the environmental conditions at IE2 are presented by Wadhams et al. (2018). Their Figures 6 and 8 show wind, wave, and ice data and the presence of eddy patterns in the ice, respectively, supporting the above description.

5.3. IE3 (RT1; 24–28 October)

The third ice-edge period IE3 is also known as Racetrack 1 (RT1), since the rectangular track that was repeated numerous times during the last 2 weeks of the cruise was established during this period. IE3 started as transit T3 exited the ice on 24 October and the ship went about 75 km SW of the ice edge, returned to the ice edge to establish a wave buoy array, and then established the repeated racetrack course on 25 October (Figure 20). The ship then completed nearly four circuits of the race track before starting ice transit T4 near 09 UTC 28 October. During period IE3, the ice edge slowly advanced toward the SW. AMSR2 shows that the entire racetrack was ice free on the first 2 days, though the ship data shows that some areas were covered by 0%–40% of very thin ice (< 2 cm) on 25 October (YD298; Figure 21c). By the end of IE3, two thirds of the racetrack was covered by 70%–90% ice concentrations with thickness of 5–15 cm. Not only did ice growth advance the edge toward the SW, but an ice tongue also protruded into the SE leg of the racetrack on 27–28 October (Figures 20d and 20e).

During IE3, the air temperature (T_a) decreased from about -5°C to about -15°C . While there is a steady decline associated with the advancing ice, semiregular variations can be seen. These represent the T_a variability associated with the ship's circuits around the racetrack, with the local T_a maxima representing

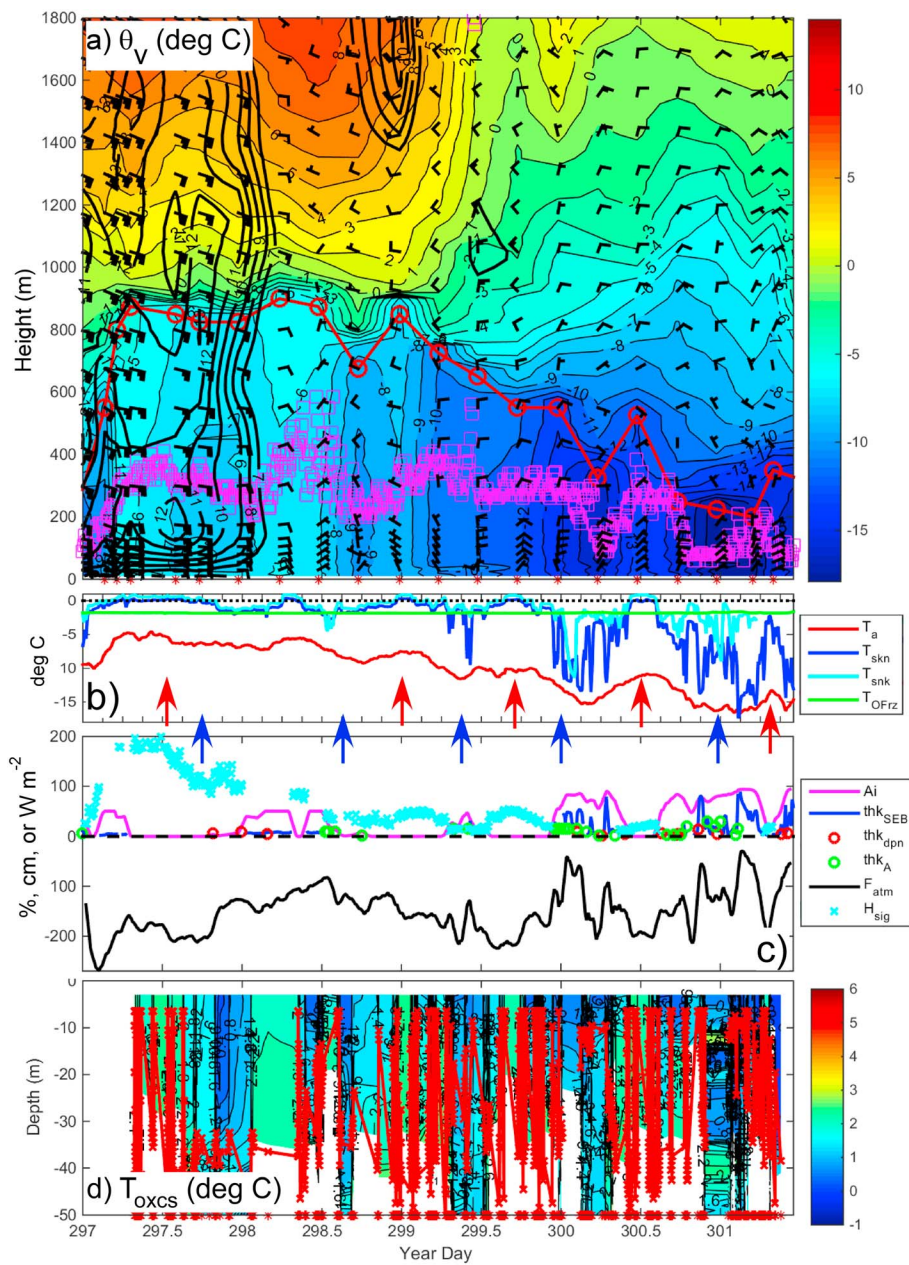


Figure 21. As for Figure 8, but for ice edge period IE3 (RT1) on 24–28 October (YD297–301). The times that the ship was located at the SW (NE) corner of the racetrack are marked by red (blue) arrows.

conditions farthest from the ice edge (generally SW corner of the racetrack). The water skin temperature (T_{skn}) farthest from the ice edge is initially near 0°C ($T_{\text{oxcs}} = +1.5^{\circ}\text{C}$) and remains at this temperature for each circuit, except for the last one (06 UTC 28 October; YD301.25) when it has decreased to the freezing point. T_{skn} is always warmer than T_a , though the difference is fairly small when the ship goes through the new ice. Significant wave height (H_{sig}) is nearly 2.0 m at the beginning of IE3 when a moderately strong LLJ with winds from the east is present over the region. However, the winds weaken as the LLJ dissipates and winds back to being between WNW and NE (having a northerly component) for the remainder of the period. H_{sig} in the open water areas later in the period are ~ 30 – 50 cm. The reduced fetch (because of northerly winds and advancing ice edge) also contributes to reducing the wave heights. The surface net heat losses (F_{atm}) are large throughout the time period (between -200 W/m^2 and -100 W/m^2) except when T_{skn} over the ice approaches T_a . Competing effects maintain this large heat loss: the increasing

air-water temperature difference compensates for the decrease in wind speed, decrease in wind/wave upper-ocean mixing, and the growth of an insulating sea ice cover. The small magnitudes of F_{atm} over the growing patches of ice suggests that the last effect will eventually reduce the surface heat loss to the atmosphere. The bulk H_s and H_l continue to be in reasonable agreement with the covariance and ID values (not shown), though there is more scatter between them during IE3 than during the ice transits. This may be because the upwind surface characteristics may be significantly different in both roughness and ice cover than those measured at the ship and used in the bulk flux calculations. These issues are being addressed in ongoing studies using this data set.

The AMLH is initially fairly high (~900 m), consistent with the AMLH found at the ice edge during the ice transits, but slowly decreases as the racetrack is covered by colder air. The air cools not just in the lowest layers but up to at least 1,800 m (top of Figure 21a) as if a different air mass moves over the site. The serial soundings show a decrease in equivalent potential temperature, which is useful as an air mass tracer, from the surface to ~800 m and from 1,000 m to 1,800 m, corroborating this assessment. The bottom of the atmosphere is heated by the heat loss from the ocean surface, and clouds persist through the entire time period with cloud bases initially at 300–400 m decreasing to 100–200 m. Cloud tops again correspond well with the AMLH as seen for the ice transits. Since the clouds are within the AML, they are heated by both the longwave radiation and turbulent heat fluxes from the surface. These two processes are then the mechanisms for transferring the ocean heat to the clouds near the top of the AMLH, where it can be lost to the upper atmosphere through cloud top longwave cooling. This cooling can then be redistributed into the AML by turbulent mixing. The lack of cooling in the lowest 800 m until the winds shift to an off-ice direction suggests that cold-air advection is necessary to overcome the strong turbulent heat flux from the open-water surfaces in this case, as the cloud top cooling is likely not sufficient. The advance of the ice can also enhance the effect of the advective cooling by reducing the heat flux from the ocean.

The OMID is highly variable for IE3 (Figure 21d), ranging from 8- to 45-m depth. This was also noted near the ice edge at this racetrack location at the end of ice transit T3 and for ice transit T4. The deep OMID is sometimes associated with near-freezing temperatures in the OML and at other times with $T_{\text{oxcs}} \sim +2^\circ\text{C}$. Large variability in OMID occurs even for periods (locations) with open water (e.g., 298.6–299.25). The general trend throughout IE3 is for the ocean temperatures to be cooling in the upper 8 m, but there is significant variability to this. Throughout IE3, there are no T_{oxcs} temperatures at any depth greater than about $+2.5^\circ\text{C}$ in contrast to the areas of warmer sub-OML temperatures seen under the ice during the ice transits, including transit T4 conducted after IE3. While the data exist to better understand the variability in the upper-ocean thermal structure seen in Figure 21d, such an analysis is beyond the scope of this overview.

5.4. IE4 (RT2; 1–4 November)

The second visit to the racetrack at the ice edge was done on 1–4 November after ice transit T4. While some excursions off the racetrack were done to deploy and recover wave buoys, all portions of the racetrack were revisited at least twice during IE4. Locations along the NW leg of the racetrack rectangle were revisited 4–6 times. During IE4, the ice edge advanced from covering only the NE corner of the racetrack on 1 November to covering the entire racetrack on 4 November (Figure 22). The ice growth near the N corner of the racetrack was slow, as low ice concentration existed in that area until 4 November. The SW corner was the last to be ice covered, reaching a concentration of 50%–70% on 4 November. While the ice edge in the racetrack area oscillated back and forth a few times during the 12 days since the end of transit T3 (23 October), this southward push of the edge was the final one for the season. On the first day of IE4, the winds backed from southerly to easterly and increased from 5 m/s to over 12 m/s (Figure 23a). The strong easterly winds persisted for the remainder of IE4 until the ship left the area late on 4 November. While ice growth was clearly occurring during IE4, significant ice advection due to the strong off-ice winds cannot be ruled out as a major contributor to the increase in ice concentration during IE4. The ice drift speed during IE4 was rapid at about 5% of the wind speed with a direction about 15° to the right of the wind (i.e., from $\sim 105^\circ$). Very little variation occurred in either drift speed or direction, likely due to the strong, steady winds.

During IE4, T_a steadily decreased from -2°C early on 1 November to -12°C at 06 UTC 2 November (Figure 23b), as the winds shifted to have an off-ice component. It then remained below -8°C until the ship moved well south of the ice edge on 4 November. This temporal evolution likely involved the various cooling and warming processes discussed for IE3; that is, cold-air advection, strong surface heat fluxes, and cloud-top

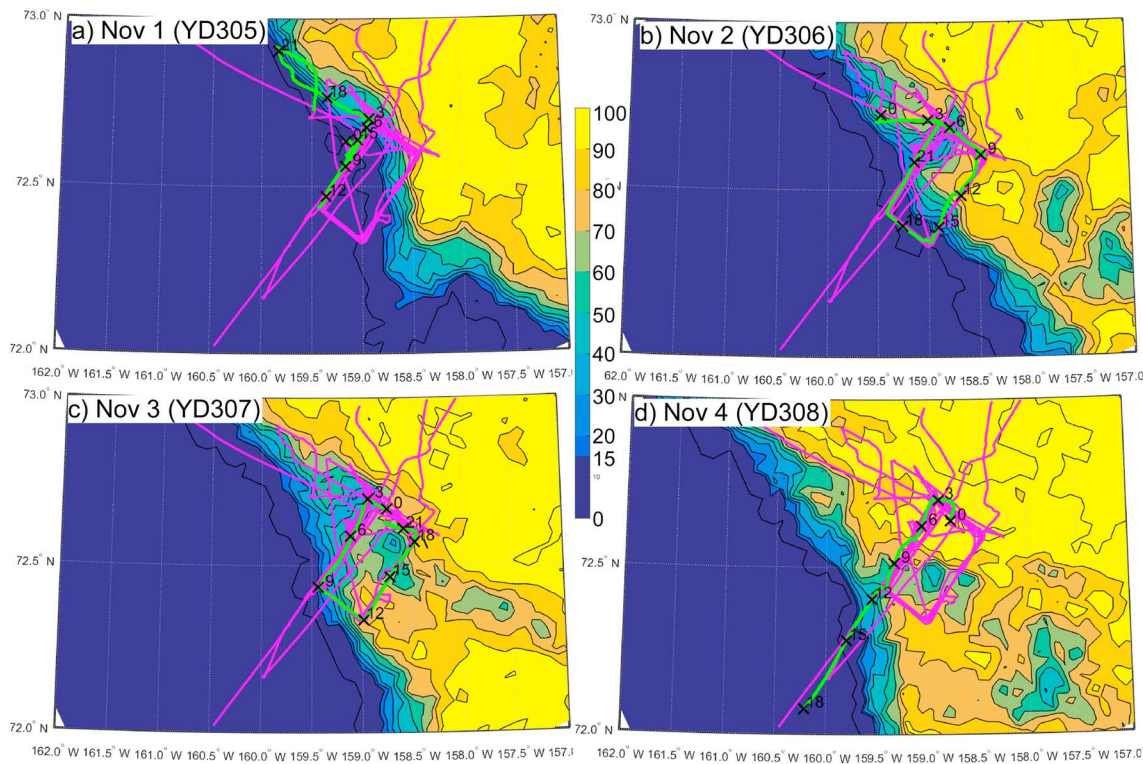


Figure 22. As for Figure 7, but for ice edge period IE4 (RT2) on 1–4 November (YD305–308).

radiative cooling. The weak warming after 09 UTC 2 November (YD306) may indicate that the very strong surface heat fluxes from the ocean overcome the cold-air advection in this case. The spatial T_a variability of $\sim 2\text{--}3^\circ\text{C}$ is illustrated by the local maxima at 12 UTC 1 November, 19 UTC 2 November, and 9 UTC 3 November, which all coincide with the ship being at the SW corner of the racetrack (see red arrows in Figure 23b). The T_{skn} varied greatly along the ship's track, being about $1\text{--}1.5^\circ\text{C}$ above the freezing point and 10°C above T_a at the SW corner to being nearly at the T_a over ice on the northern side of the racetrack. When combined with the strong winds, very large heat losses occurred over the warm open water areas and even over thin ice with relatively warm T_{skn} . F_{atm} of -400 W/m^2 occurred during some periods and locations (Figure 23c), while F_{atm} of -70 to -30 W/m^2 occurred over the thicker ice areas. Hence, heat was rapidly being lost from the upper ocean in areas with no ice on the surface. In such areas, not only was F_{atm} large but the significant wave heights were between 1 and 2 m because of the strong winds despite the short fetch (e.g., 19 UTC 2 November; YD306.8; Figure 23c; see also Figure 22b). While the strong winds contributed to the large surface heat losses, the wind-driven upper-ocean mixing they cause may have increased the heat reservoir from which this surface heat loss occurs. This may have helped maintain a relatively warm T_{skn} despite strong cooling. Note that T_{skn} at the SW corner shows little or no cooling trend until ice has formed on the ship's last pass over that location, as also occurred for IE3.

During most of IE4, the AMLH varied between 250 m and 800 m, with some indication that the lower heights occur at the northern end of the racetrack within the ice. It was cloudy most of the time, though with some breaks early on 1 November (SW corner) and 2 November (NE corner). The cloud bases were mostly 50–250 m below the AMLH, with tops close to the AMLH. Some higher cloud bases occurred early on 1 November and late on 3 November. While the low-level cold air was similar to what developed during the latter part of IE3, θ_v warms above 1,000 m for IE4 in contrast to what occurs during IE3. These upper level changes were therefore likely more related to the synoptic evolution rather than to the presence of surface ice and the surface energy fluxes.

Another distinct difference for IE4 compared to IE3 is the presence of a LLJ through the entire period. At least 4 LLJ cores exist in the time-height cross section (Figure 23a), with the cores either coinciding with or

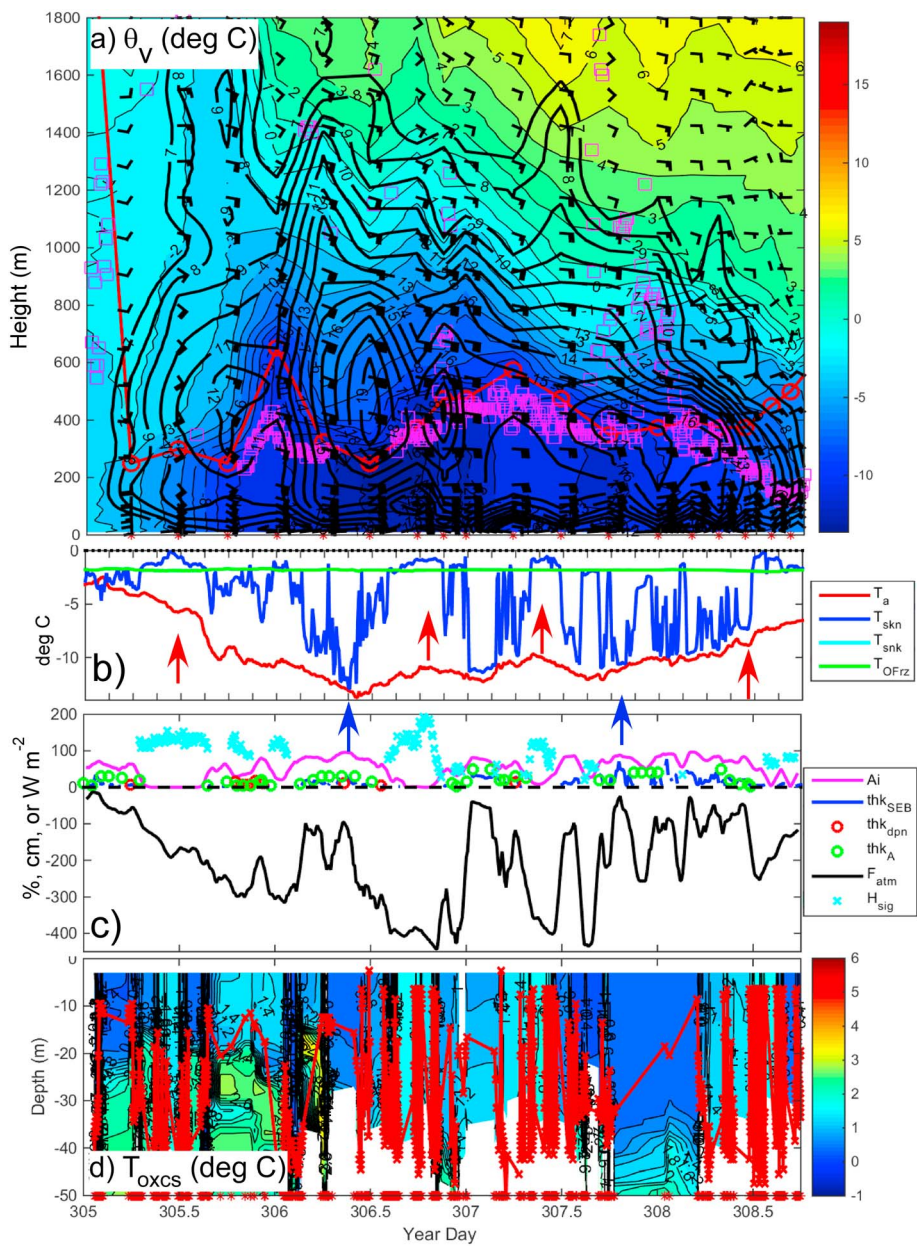


Figure 23. As for Figure 21, but for ice edge period IE4 (RT2) on 1–4 November (YD305–308).

occurring just above the local AMLH. Analysis of the structure and dynamics of this LLJ is presented by Guest et al. (2018).

The OMID again shows very large variability for this racetrack area as seen for IE3, with OMID varying between 8 m and 45 m. T_{oxcs} in the OML is $\sim +1$ to 2°C near the SW corner, while it is $\sim +0.1$ to 0.3°C near the NE corner. Some areas with ice cover show $T_{oxcs} \sim 0.0^\circ\text{C}$, though others show T_{oxcs} is $\sim +0.5$ to 1.4°C . Clearly, a more detailed analysis is needed to understand this variability.

6. Discussion

The shipboard observations of the air, ice, and ocean during Sea State are many and varied, as described in section 2. In sections 4 and 5, we juxtaposed many of these parameters during four transits through the ice and four other time periods while at the ice edge to reveal and suggest numerous air-ice-ocean interaction

processes during the important autumn freezeup period, revealing many processes that recurred, as well as some that did not. The key structures and dominant processes during autumn freezeup are discussed in this section, using the individual transit and ice edge observations and composites or averages of the data. In particular, the air-ice-ocean structure and processes over the interior of this new and thin sea ice differ substantially from those over open water near the ice edge, even only a few days after ice formation. To focus on the distinct interior-ice and open-water portions of the data, averaging is done by selecting only points where $Ai > 35\%$ and distance to the ice edge is greater than 10 km for the former and $Ai < 15\%$ for the latter. This represents a subset of the transit and ice edge data examined in sections 4 and 5. The early portion of transit T1a occurred over open water and therefore qualifies as an ice edge period (IE0) through the above criteria. Because ice edge periods alternate with transits, the average or composite data are used to examine the temporal evolution over the 5-week period of structures over the ice interior and at the ice edge, as well as illustrate the environmental differences between the ice edge and the interior. Table 5 shows the means of many parameters for the open-water ice edge or ice interior periods. The values are discussed below.

6.1. Atmospheric Structure and Processes

While analysis of the individual transits and ice edge periods suggest significant differences in the lower troposphere between the ice edge and ice interior, the mean θ_v profiles in the ice interior and bracketing open water periods quantify these differences (Figure 24). In general, the atmosphere below 300–1,000 m is 3–8°C colder over the ice interior compared to the ice edge open water. This is slightly less than the 1,400- to 1,850-m height of the wintertime impact of thin ice determined from a modeling study (Rinke et al., 2006). Furthermore, the atmospheric mixed layer depth, as indicated by the depth of the layer of constant θ_v , is much shallower over the ice than over nearby open water, being generally less than 250 m over ice and up to 1,600 m over open water. The 50- to 250-m AMLH over thin FYI is consistent with wintertime measurements in the MIZ over seasonal ice during MIZEX-West (Overland, 1985). Similarly, the cloud base is lower over ice than over open water, though the cloud fraction (Table 5) is significantly higher over open water. This provides a physical basis for the previous finding that the autumn cloud base over the open water of the Chukchi Sea in the 2000s was higher than during the ice-covered period in 1998 (Sato et al., 2012). Over both ice and open water, the low cloud base suggests the frequent presence of low-level stratocumulus clouds with bases below the AMLH and the capping inversion. Over the ice, the AMLH is very shallow for transits T1b and T3, coinciding with very low cloud fractions, suggesting that the absence of clouds suppresses the surface turbulent fluxes, enhances the longwave cooling, and leads to shallower AMLHs. Superadiabatic lapse rates occur in the lowest few tens of meters over both the open water and the ice interior, though the air surface temperature difference is greater over open water (Table 5). That is, the ice-open water temperature difference is greater for the surface temperature than for the near-surface air temperature. While Figure 24 summarizes the key characteristics, significant variability in both thermal profiles and cloud characteristics were present between individual soundings, as seen in sections 4 and 5.

The sea level pressure is generally higher over the ice interior than at the ice edge (Table 5), which is consistent with ice-interior cooling. This gradient likely promotes off-ice winds, which occurs in four of the five ice edge periods (negative WD-IEor in Table 5). As seen in the individual cross-sections in sections 4 and 5 and discussed by Guest et al (2018), the higher near-surface wind speed at the ice edge is partially due to the presence of one of two types of ice edge low-level jets (density current and thermal wind generated), both produced by the thermal and pressure gradients between the ice interior and open water at the ice edge. Mean ice edge significant wave heights ranged between 44 cm and 3.4 m, with the largest waves associated with the only ice edge period with on-ice winds (positive WD-IEor in Table 5) and on-ice waves (positive WVd-IEor) on 11–12 October. Two other cases primarily had a component of off-ice winds but approximately ice edge-parallel wave directions (negative WD-IEor and small WVd-IEor in Table 5), since the waves move to the right of the wind (positive WVd-WD in Table 5). Part of one period (IE2) had a directly off-ice wind with corresponding directly off-ice wave direction. Because the ship's research priorities included measuring ice-wave interactions, the ship was preferentially present at the ice edge at times forecasted to have stronger winds and larger waves. Hence, the ice edge winds and waves are likely biased higher in this data set than they might be in a data set with continuous ice edge measurements.

In general, the lower tropospheric temperature decreases with time during the 5-week field deployment over both the ice interior and the open water (Table 5 and Figure 25a). Transit T2 is an exception to this general

Table 5
Average or Median Values of Various Parameters for Ice Edge Open Water Locations (IE, $Ai < 15\%$) and Ice Interior Transits (T, $Ai > 35\%$) and Ice Edge Distance > 10 km)

Parameter	IE0	T1a	T1b	IE1	T2	IE2	T3	IE3	T4	IE4	Tavg	IEavg
Mean day of year	277.35	278.68	282.32	285.14	288.72	291.84	294.3	298.76	302.96	306.48		
Date range (DDDHH-DDDHHH)	27703-27711	27805-27905	28106-28322	28400-28514	28711-29000	29117-2921	29202-29705	29707-30011	30506	30816	30512-	
Number of data hours	16	27	61	15	54	5	25	10	16	4	14	22
Number of soundings	4	5	13	4	10	2	56	74	19	67	5	
17-m air temp (T_a , °C)	-2.2	-6.5	-7.8	-3.7	-3.8	-6.9	-14.3	-8.3	-16.3	-7.9	-9.7	-5.8
Skin temp (T_{skn} , °C)	-1.5	-3.6	-5.2	-1.5	-1.1	-1.1	-12.5	-0.7	-13.4	-1.1	-7.5	-1.2
$\Delta T = T_a - T_{skn}$ (°C)	-0.7	-2.9	-2.6	-2.2	-0.9	-5.8	-1.8	-7.6	-2.9	-6.8	-2.2	-4.6
Sea level press (hPa)	1018	1022.8	1020.9	1001.7	1016.7	1016.5	1025	1018.5	1014.1	1003.8	1019.9	1011.7
Wind speed (WS, m/s)	4.7	4.3	2.6	13.6	0.9	9.2	3.3	4.2	3.9	9.8	1.7	5.6
Wind dir (WD, deg from)	332	46	333	104	238	12	36	64	117	103	48	70
Ice edge orien (IEor; deg off ice < 0, on-ice > 0)	129	n/a	n/a	24	n/a	121	n/a	126	n/a	146	n/a	109
WD-IEor (deg; off ice < 0, on-ice > 0)	-23	n/a	n/a	80	n/a	-109	n/a	-62	n/a	-43	n/a	-31
Cloud fraction (%)	80	81	47	100	81	88	44	100	83	100	67	94
Median cloud base cello (m)	690	235	320	500	470	805	270	300	240	430	315	545
Mean cloud base sounding (m)	1130	205	405	488	410	920	260	310	375	260	330	622
Atmospheric Mixed-Layer Height (AMLH, m)	738	315	448	867	617	312	198	735	354	406	429	612
F_{atm} (W/m ²)	-39.4	-60.1	-77.2	-93.3	-52.2	-168.9	-74.4	-170.8	-73.3	-256.8	-67.4	-145.8
H_s (W/m ²)	5.7	25.2	22.3	36.8	6.5	83.3	23	84.4	28.5	132.2	21.1	68.5
H_t (W/m ²)	11.7	13.5	13.2	43.6	6	48.9	9.8	49.8	9.1	75.2	10.3	45.8
LW_n (W/m ²)	-37	-39.9	-58	-16.5	-51.4	-60.9	-43.8	-38.9	-37.2	-49.6	-46.1	-40.6
SW_n (W/m ²)	14.9	17.8	16.3	3.6	11.6	24.2	3	2.4	1.6	0.2	10.1	9.1
Ustar (m/s)	0.16	0.18	0.18	0.52	0.17	0.34	0.15	0.25	0.19	0.45	0.17	0.34
Composite ice conc. (A_i , %)	1	76	80	5	82	3	95	2	94	3	85	3
Median ice thick-ASSIST (cm)	125	15	13	2	20	0	25	1	30	0	21	26
Median ice thick - SEB (cm)	0	7	10	0	5	0	37	0	38	0	19	0
Median snow thick (cm)	0	0	0	0	2	0	2	0	2	0	1.2	0.0
Ice drift speed; IDs [m/s, (km/day)]	0.05	0.06	0.12	0.26	0.12	0.65	0.12	0.12	0.34	0.21	0.15	0.26
Drift ratio = IDs/WS (%)	1.1	1.4	4.7	1.9	13.2	7.0	3.7	3.0	8.8	2.1	6.4	3.0
Drift Dir (IDd; deg CW from N)	(4.6)	(5.3)	(10.6)	(22.3)	(10.3)	(55.8)	(10.6)	(10.7)	(29.5)	(18.1)	(13.3)	(22.3)
IDd-WD (deg; to R > 0; to L < 0)	356	113	337	136	163	56	101	19	122	125	117	77
IDd-IEor (deg; on ice > 0, off-ice < 0)	24	67	4	32	-75	44	65	-45	5	22	69	7
Sig. wave height (H_{sig} , m)	0.47	n/a	n/a	112	n/a	-65	n/a	-107	n/a	-21	n/a	-26
Wave dir (WWD; deg from, CW from N)	n/a	n/a	n/a	3.37	n/a	0.44	n/a	0.78	n/a	1.22	n/a	1.26
WWD-WD (deg; to R > 0, to L < 0)	n/a	n/a	n/a	22	n/a	173, -2	n/a	65	n/a	225, 127	n/a	78
WWD-IEor (deg; on-ice > 0, off-ice < 0)	n/a	n/a	n/a	102	n/a	64, -111	n/a	3	n/a	79, -19	n/a	-5
Ocean mixed-layer depth (OMLD, m)	-14	-16	-23	-23	-20	-12	-12	-27	-15	-32	-17	-22
Std. dev. OMLD (m)	5.1	4.1	2.5	4	6.3	2.2	5.9	8.9	8.9	6.8	5.5	5.4
Salinity (S, psu)	27.7	26.9	26.8	27.1	26.8	31.3	27.6	33.2	29.1	33.7	27.4	30.6
Std. dev. S (psu)	0.3	0.4	0.2	0.2	0.3	0.5	1.4	0.4	1.2	0.7	0.7	0.4

Note. Ice edge (IEavg) and interior (Tavg) averages are shown in the last two columns. Some cells in rows involving wave direction (Wwd) have two values, indicating that changes occurred during the IE period. ASSIST = Arctic Shipborne Sea Ice Standardization Tool; SEB = surface energy budget.

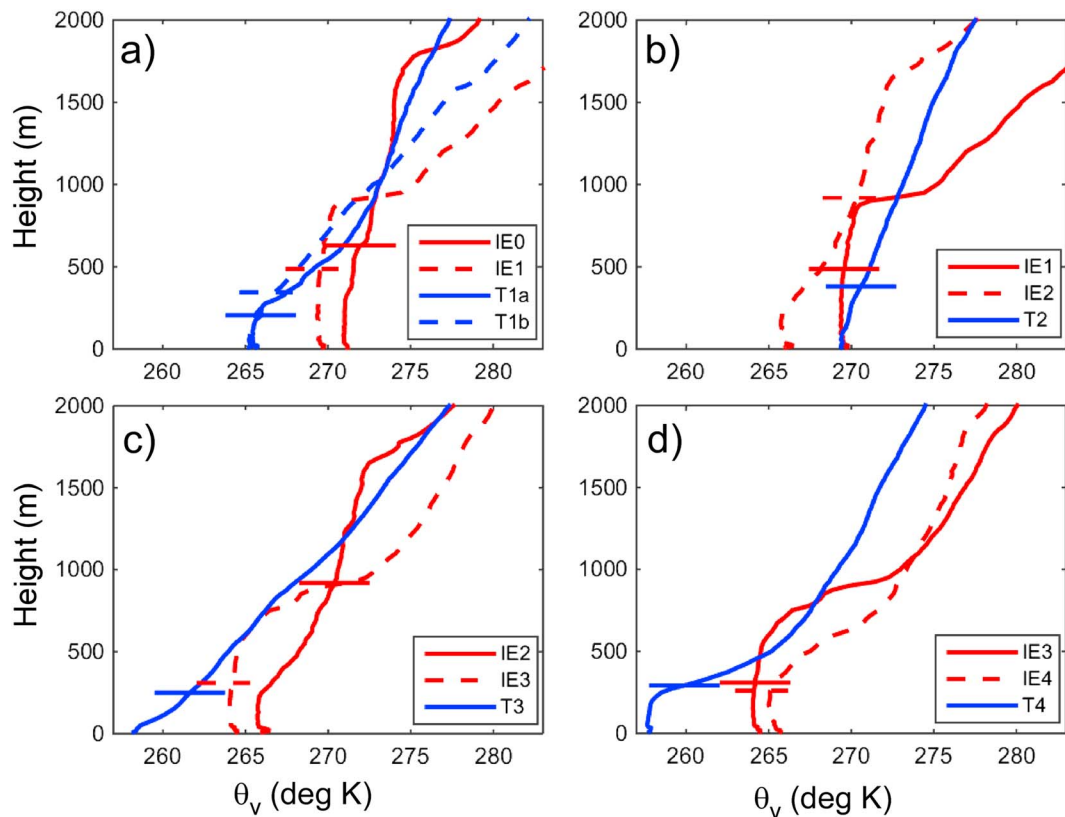


Figure 24. Mean atmospheric profiles of virtual potential temperature (θ_v) for each of the four transits (a) T1, (b) T2, (c) T3, and (d) T4 (blue) and the bracketing ice edge periods (red). The mean cloud base for each profile is shown as the horizontal bar.

seasonal cooling trend and is likely due to the influence of the strong on-ice advection occurring on 10–14 October (IE1) and a subsequent transient weak cyclone impacting the ice interior in contrast to dominant off-ice flow and high-pressure systems for the other ice interior periods (see Figure 5a). The cooling of T_a from -6°C to -16°C over the ice interior over ~ 28 days is due to the cooling of the ice surface by a similar amount (-5 to -3°C to -13 to -12°C) and occurs as the interior ice thickens from 5–10 cm to 25–40 cm. Hence, the air-surface temperature difference ($\Delta T = T_a - T_{\text{skn}}$) does not change much, and an unstable surface layer is maintained over the interior ice throughout the freezeup process. In contrast, there is no cooling of the open water surface at the ice edge. Instead, the cooling of the air over the open water results from the cooling over the ice interior and development of off-ice airflow over the open water adjacent to the ice, as represented by the negative values of WD-IFor for four of the five IE periods (Table 5). This results in a substantial increase in the magnitude of ΔT over time (Figure 25a), and the atmospheric surface layer at the ice edge becomes more unstable as freezeup progresses. The ultimate reason for this destabilization at the ice edge is the development of the very cold air over the ice interior and off-ice, cold-air advection over the unfrozen water surfaces, leading to an enhanced temperature differential between the ice edge and ice interior. Basic dynamical considerations suggest that this off-ice airflow should become more persistent as the ice interior cools, and that baroclinic LLJs become stronger and shallower.

Additional insights into the freezeup process can be found by examining the evolution of the means of some of the surface energy budget terms (Table 5 and Figure 25b). Over the ice interior, the net heat loss (F_{atm}) from the surface to the atmosphere remained between 52 and 77 W/m² during the entire field program, even after the ice thickened. This heat loss represents heat conducted through the ice (and snow cover if present) coming from either the latent heat of fusion from ice growth at the bottom of the ice or heat flux to the ice from the ocean below.

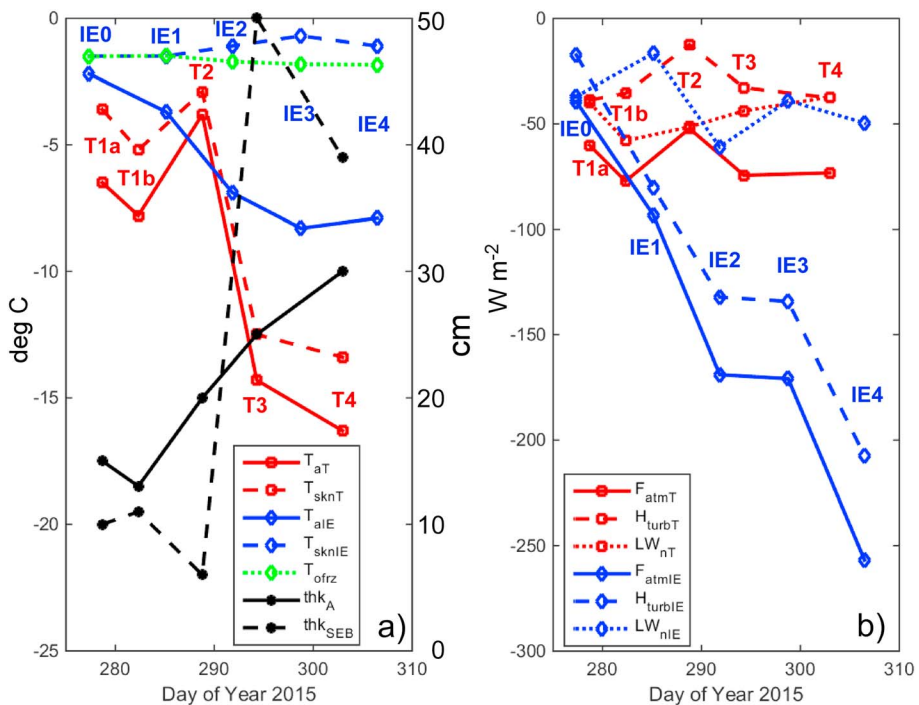


Figure 25. Evolution of statistics of key parameters for each of the transits and ice edge periods during Sea State. Shown are (a) T_a , T_{skn} , ice edge ocean freezing point, and ice thickness; and (b) F_{atm} , H_{turb} ($= -H_{sb} - H_{lb}$), and LW_n . Red curves are for the transits (ice interior) and blue the ice edge (open water). For improved clarity, the sign convention of total turbulent heat flux (H_{turb}) has been reversed.

Furthermore, this surface heat loss is potentially an atmospheric heat gain, so one needs to explain the cooling of the air over the ice interior in this context. Approximately two thirds of F_{atm} over the ice interior is due to longwave radiative cooling, while the remaining one third is due to turbulent heat flux. The turbulent heat component is transported toward the top of the atmospheric mixed layer (AMLH), and, when mixed-phase clouds occur near the AMLH, longwave radiation from the surface will also be absorbed near the AMLH (~ 200 – 600 m). If we assume that the cloud top radiative cooling of $F_{rad_CT} = -80$ to -100 W/m^2 observed by Pinto (1998) in middle-to-late October near the Beaufort Sea ice edge is representative of the cloud top radiative heat loss over the ice during Sea State, the AML will have a net heat loss of 3 – $48 \text{ W/m}^2 (F_{atm} - F_{rad_CT})$. This cooling, occurring at cloud top, would be redistributed within the AML by turbulent eddies from *upside-down* convection associated with the clouds (e.g., Solomon et al., 2011). If skies are clear, the enhanced longwave cooling of the surface would stabilize the surface layer if the surface longwave cooling exceeds the heat conducted through the ice, suppressing the turbulent heat flux, and lead to a small or even positive ΔT . This occurred on a few days in transits T1b, T2, and especially T3, with correspondingly small H_{turb} and very low (~ 100 m) AMLH. This discussion of the cooling mechanism is speculative because of the lack of more detailed cloud and cloud top cooling observations, but is consistent with the Sea State observations for the individual transits as well as for the mean structures in Figure 24.

Over open water at the ice edge, the magnitude of F_{atm} increases throughout the field campaign (Figure 25b). This increase is almost entirely due to an increase in H_{turb} , as LW_n is quasi-constant near $-41 \text{ W/m}^2 (\pm 20 \text{ W/m}^2)$ while H_{turb} increases from 17 W/m^2 to 207 W/m^2 . This increase in H_{turb} is due primarily to the decrease in T_a and increase in the magnitude of ΔT , as discussed previously. Hence, the large heat losses at the ice edge toward the end of the field program are also due to the cooling of the AML over the interior of this growing FYI, though through a series of indirect processes. The strong winds associated with the LLJ during IE4, itself likely produced by the cooling in the ice interior, also contributes to the large F_{atm} at this time.

Lower atmospheric heating and cooling processes over the ice edge open water areas are similar to those over the ice interior discussed above, but the ocean-atmosphere heat fluxes of $\sim 200 \text{ W/m}^2$ or more are

much larger than the ice-atmosphere fluxes over the interior, thereby producing stronger boundary layer heating, deeper mixed layers, and more frequent cloudy conditions. The larger heat fluxes over the open water may be large enough to at least cancel, if not reverse, the cloud top cooling effect, assuming that it is similar to that over the ice interior, thereby requiring off-ice cold-air advection in order to cool the atmosphere over the ice-edge open water, as seen for both IE3 and IE4. For cases like IE4, the surface turbulent heat fluxes may be large enough to even warm the lower atmosphere slightly despite the cold-air advection. Evaluating the balance between these processes requires measurements of the cloud top cooling not available for this study and likely would be best accomplished using a numerical process model.

6.2. Ice Characteristics

Ice thickness in the ice interior increased from 10–12 cm to 25–50 cm (Figure 25a). The differences between the thickness estimates are likely due to the subjective nature of the manual ASSIST technique and the overestimation due to some snow cover for the SEB technique. These changes provide an estimated ice growth rate of 0.5–1.6 cm/day, which is equivalent to a latent heat of fusion loss of 14–44 W/m². This is less than the $F_{\text{atm}} = -77$ to -52 W/m² heat loss estimated from the surface flux estimates, but the heat flux difference of 8–63 W/m² is likely contributed from the upper ocean below the sea ice.

The mean ice drift speeds ranged from 1.1% to 13.2% of the wind speed, with a larger drift speed ratio in the thin-ice interior than for the low ice concentration areas near the ice edge (Table 5). The drift velocities are 68% greater at the ice edge because the wind speeds are stronger there. The mean drift-wind direction differences (IDd-WD) suggest that the ice generally drifts to the right of the wind as expected, though there are several periods where the mean drift is to the left of the wind. Furthermore, the detailed time series discussed in section 4 showed significant variability of both the drift ratio and IDd-WD. This large scatter in the drift speed ratio and inconsistent wind-relative drift direction are likely due to forcing of the ice drift by processes other than the wind, such as by ocean currents. Near the ice edge, with one exception, the mean ice drift was generally off-ice because of the frequent off-ice wind component and the irregular wind-ice drift correlation; that is, the ice tended to drift into the open water near the ice edge, enhancing the southward advance of the ice otherwise due to ocean freezeup. The Sea State ice drift characteristics are discussed in more detail by Lund et al. (2018).

6.3. Upper-Ocean Characteristics

The sequence of cooling and heating mechanisms for the atmosphere discussed above is also responsible for the loss of the upper-ocean heat, as this heat is transferred to the lower atmosphere either directly from the water surface or by conduction through the thin ice cover. This heat loss can be increased by strong ice edge winds (e.g., LLJ), which would also increase the ocean mixing and hence the upward transport of heat within the ocean. The formation or advection of an ice cover as seen in both the ice interior and the ice edge locations, will reduce the ocean heat loss to the atmosphere and also likely reduce the upper-ocean mixing, the latter suppressing heat transport to the bottom of the ice. While upper-ocean turbulent mixing was not measured during Sea State, warm temperatures well above the freezing point were seen within 8–15 m of the bottom of the ice, such as during transit T4, and may represent near-surface warm water that is unable to transfer its heat to the ice sufficiently rapidly to overcome heat loss from the ice to the atmosphere.

While the lower atmospheric structure appears to be clearly linked to the formation and presence of sea ice, the upper-ocean thermohaline structure is not as clearly linked. The depth of the ocean mixed layer (OMLD), the thermal structure below the OMLD, and variability of the OMLD appear to be more associated with the bathymetry of the Sea State region. Water under the ice in the Canada Basin (e.g., transit T1b) had a fairly uniform OMLD of ~23 m (see Figure 9 and Table 5), with the water within the OML being very near its freezing point. A weak NSTM existed just below the OMLD and a layer of likely Pacific water was present at ~60-m depth. Some pulses of very warm water were also noted in the Canada Basin, though closer to the Chukchi Shelf (transit T2). Such warm water was also found a little higher in the water column (40- to 60-m depth) near the corner of the Chukchi Cap, Chukchi Shelf, and Canada Basin (transits T1a, T2, and T3). For the transits that included transects from the Chukchi Shelf to the Chukchi Cap (T1a, T3), it was found that the OMLD was very shallow in this region, and the water just below the OMLD had warm patches with significant variability. The water on the Chukchi Shelf just above the bathymetric precipice into the Canada Basin, was sampled with the end of transit T3, transit T4, IE3, and IE4. All of them showed a highly variable

OMLD (Table 5), varying between 8 m and 45 m for individual CTDs and means of 12–32 m (standard deviations of 6–9 m). A shallow OMLD was seen under the ice for the transits and deeper values for the open-water ice edge periods. In some patches under ice, water significantly above the freezing point is only 8–10 m below the surface, such as seen in Figure 19 for transit T4. Salinity is higher in the open water areas at the ice edge than under the ice during the entire cruise, which is one consistent difference between the upper ocean in the ice interior compared to the ice edge. However, it is unclear whether this salinity difference is produced by the ice formation or corresponds to a background regional pattern of salinity as reported by Timmermans et al. (2014).

We speculate that ocean eddies induced by the shelf break (e.g., Häkkinen, 1987) have produced these distinct upper-ocean characteristics at the racetrack location, as well as possibly over the slope between the Chukchi Shelf and Chukchi Cap. Furthermore, oceanic eddies are likely to form at ice edges due to processes such as differential momentum fluxes, differential surface heating, and bottom melt (e.g., Häkkinen, 1986; Horvat et al., 2016). Eddies at the ice edge and along the shelf break were noted in synthetic aperture radar imagery on several occasions during Sea State (e.g., see Figure 8 of Wadhams et al. (2018) for an example from IE2). The smaller scale of ocean eddies compared to atmospheric eddies may be one reason why the ocean variability appears greater in these areas.

A key objective of Sea State was to improve understanding of wave-ice interactions during the autumn freezeup. The significant wave heights (H_{sig}) encountered in the open water at the ice edge during Sea State varied significantly. By far the largest waves encountered were during the on-ice strong-wind event of IE1, with mean H_{sig} of ~3.4 m and periods with H_{sig} approaching 5 m (Table 5). The waves propagated 22°–65° to the right of the wind for three of the four IE periods, and slightly to the left during IE2. These differences in the wind-relative orientation of the waves are likely due to a nonlocal forcing of some of them, especially for the longer wavelengths. Because the winds had an off-ice component for all but one of the IE periods, the waves were generally either off-ice or ice-parallel, even for IE2, so the fetch was often limited for wave growth. The strong on-ice winds produced large on-ice waves for IE1, but this case was the exception during the Sea State cruise. Despite the off-ice character of the waves for IE3 and IE4, the open water portions of the racetrack (Figures 20, 21, 22, and 23) with the greatest fetch from the ice edge had H_{sig} values of 1.5–2.0 m, with mean values of 0.8–1.2 m (Table 5).

One might expect that the large F_{atm} seen during IE3 and IE4 would lead to rapid cooling of the upper ocean and freezeup, and it is tempting to attribute the final freezeup shown in Figure 22d to this heat loss. However, despite many days of large F_{atm} , T_{skn} did not cool significantly for some open water areas of the racetrack. This can be seen for the T_{skn} for the SW corner of the racetrack in Figures 21 and 23. This can only occur if the surface heat loss is offset by heat flux of comparable magnitude to the ocean surface from below. As done previously in trying to explain the large variability in OMLD during IE3 and IE4, we again speculate that small-scale ocean eddies exist over the Chukchi Shelf break that transfer significant heat to the surface. The average ice drift speed during IE4 was 18.1 km/day, which was greater than at any other time during the field program. The ice drift during IE4 also averaged 22° to the right of the wind, which in turn was very steady and averaged coming from 103°. Since the ice edge was oriented at 326°–146° (e.g., Figure 22b), the ice drift had an orientation that was 21° into the open water area. That is, during IE4, the ice drift perpendicular to the ice edge was 6.5 km/day. Hence, during the 3 days of IE4, the 20-km drift alone could explain ~55%–60% of the change in ice cover. If ice drift is important for the ice edge advance into a region with significant heat flux from below, one might expect that ice advected into this region would at least partially melt, producing shallow layers of relatively fresh water. This could also contribute to the highly variable OMLD noted before and significant variability in salinity (Table 5). The introduction of ice through drift or surface freezing could also shut off the wind-mixing mechanism of the upper ocean, producing a dynamic impact on the upper-ocean structure. Clearly, extensive further analysis is needed to understand the complex air-ice-ocean interaction processes occurring in the racetrack region.

7. Conclusions

This study summarizes the numerous in situ measurements of the near-surface atmosphere, surface characterization, and upper-ocean thermal and salinity structure obtained by an icebreaker as the Beaufort and Chukchi Seas cooled and sea ice formed in autumn 2015. We have described some of the key data

processing steps and the derivation of many atmospheric, ice, and upper-ocean parameters, including surface energy budget terms. The number of parameters measured or derived are large and the location and time of year of the data collection is unique. Hence, the shipboard observations from the Sea State field program produced a unique air, ice, ocean data set for describing the near-surface environment during autumn freezeup.

The data were analyzed by taking advantage of alternating ice edge and ice transit observation periods during Sea State and separating the observations over the new thin (<50 cm) first-year ice from those near the ice edge in two slightly different ways. The results have been discussed in sections 4–6. The main conclusions are as follows:

1. Significant cooling occurred in the lowest 800–1,000 m of the troposphere within a few days of ice formation through weaker surface radiational and turbulent heat fluxes (less tropospheric warming) compared to the adjacent open water areas. Cloud top cooling is likely an important component of this process, though not measured in this study.
2. This cooling continued through the autumn, strengthening the atmospheric baroclinicity at the ice edge, which in turn led to several feedbacks, such as off-ice atmospheric flow, the frequent formation of ice edge low-level jets, the dramatic destabilization of the atmospheric surface layer over the adjacent water, and the enhancement of the oceanic heat loss to the atmosphere through turbulence over this adjacent water. The off-ice cold-air advection acted as a negative feedback on the development of the ice edge baroclinicity, damping the increase of the ice-open water near-surface air temperature gradient.
3. The ice growth rate (thickness increase) over the ice interior is consistent with the observed surface energy fluxes of ~ 65 W/m 2 , with the inclusion of estimates of oceanic heat flux to the ice bottom and cloud top radiative cooling. Surface cooling of open water areas near the ice edge was not observed despite the large surface heat fluxes of 200 W/m 2 or more, suggesting that upper-ocean mixing due to effects from strong winds at the ice edge or ocean eddies effectively mixed heat to the ocean surface.
4. While the tendency for higher wind speeds at the ice edge produced more rapid ice movement there, the observations suggest that ice drift was also significantly forced by oceanic currents or eddies and the Coriolis term (inertial forcing).
5. Observed significant wave heights with moderate-to-strong winds at the ice edge ranged from 20 to 200 cm to nearly 5 m, depending on whether winds were off-ice or on-ice and the fetch from the ice edge for the former.
6. Variability of upper-ocean thermal and salinity structure, including mixed-layer depth, seemed to be related to bottom bathymetry, the presence of small-scale oceanic eddies, the apparent upper-ocean wind mixing and its rapid suppression upon ice formation, and a possible role of an ice-advection/bottom melt process. Evidence suggesting these processes include the presence of warm water just 8–15 m below the forming ice; ice drift angles and speeds inconsistent with observed surface winds; small-scale variability of upper-ocean temperature, salinity, and mixed-layer depth; and the lack of surface cooling in open water despite rapid heat loss to the atmosphere. Very small scale, large-amplitude thermal variability occurs near the surface over the Chukchi Sea shelf break, including large variability of the ocean mixed-layer depth. This is in stark contrast to the very uniform ocean mixed-layer depth over the Canada Basin, both under the ice and in a small open water area.

Acknowledgments

The Sea State Directed Research Initiative was supported by the Office of Naval Research, Code 32, under program managers Scott Harper and Martin Jeffries. ONR support for O. P., B. B., P. G., and C. F. was provided through grants N00014141P20038 and N000141612018, for J. T. by N00014-13-1-0284, for S. A. by N000141310435, for S. S. by N000141310434, for B. L. by N00014-13-1-0288, and for L. R. by N00014-15-1-2744. Some of the analyses by O. P., B. B., and C. F. were also supported by funds from the National Oceanic and Atmospheric Administration. We appreciate the great efforts made in collecting this data set, including those of the Sea State science staff and the crew of the R/V *Sikuliaq*. Ian Brooks kindly lent us the Heitronics KT15s used in this study. For more information and access to the data, please refer to the Sea State website (www.apl.washington.edu/arcticseastate) and use the Data tab.

Differentiation between spatial and temporal variability is at times difficult with this data set, as demonstrated by the analysis presented. However, no other characterization exists of the structure and variability of lower troposphere and upper ocean in context of the evolving surface characteristics at this time of year over the Arctic Ocean. The description of the data processing provides necessary background for various studies that use or will use components of this data set for specific studies. Furthermore, this study broadly characterizes this rarely sampled environment with numerous air-ice-ocean parameters, and identifies features, characteristics, or processes that warrant further detailed analysis, such as the complex shelf-break upper-ocean variability and freezeup, and the relationships between turbulent fluxes and the complex surface conditions. Such analyses are left to future studies.

References

- Andreas, E. L., Horst, T. W., Grachev, A. A., Persson, P. O. G., Fairall, C. W., Guest, P. S., & Jordan, R. E. (2010). Parameterising turbulent exchange over summer sea ice and the marginal ice zone. *Quarterly Journal of the Royal Meteorological Society*, 136B, 927–943.

- Blomquist, B., Persson, O., Fairall, C., & Pezoa, S. (2015). SKQ201512S/SeaState DRI: Brief analysis of bulk Met observations. NOAA/PSD Internal Report, Nov. 2015 (available at ftp://ftp1.esrl.noaa.gov/psd3/cruises/SeaState_2015/Met%20Report)
- Briegleb, B. P., Bitz, C. M., Hunke, E. C., Lipscomb, W. H., Holland, M. M., Schramm, J. L., & Moritz, R. E. (2004). Scientific description of the sea ice component in the Community Climate System Model, version three. NCAR Tech. Note NCAR/TN-463_STR, 70 pp.
- Collins, C. O. III, Blomquist, B., Persson, O., Lund, B., Rogers, W. E., Thomson, J., et al. (2017). Doppler correction of wave frequency spectra measured by underway vessels. *Journal of Atmospheric and Oceanic Technology*, 34(2), 429–436. <https://doi.org/10.1175/JTECH-D-16-0138.1>
- Edson, J. B., Jampana, V., Weller, R. A., Bigorre, S. P., Plueddemann, A. J., Fairall, C. W., et al. (2014). On the exchange of momentum over the open ocean. *Journal of Physical Oceanography*, 44(9), 1589–1610.
- Fairall, C. W., Bradley, E. F., Godfrey, J. S., Wick, G. A., Edson, J. B., & Young, G. S. (1996). Cool skin and warm layer effects on the sea surface temperature. *Journal of Geophysical Research*, 101, 1295–1308.
- Fairall, C. W., Bradley, E. F., Hare, J. E., Grachev, A. A., & Edson, J. B. (2003). Bulk parameterization of air-sea fluxes: Updates and verification for the COARE algorithm. *Journal of Climate*, 16, 571–591.
- Fairall, C. W., Bradley, E. F., Rogers, D. P., Edson, J. B., & Young, G. S. (1996). Bulk parameterization of air-sea fluxes for TOGA COARE. *Journal of Geophysical Research*, 101, 3747–3764.
- Fairall, C. W., & Markson, R. (1987). Mesoscale variations in surface stress, heat fluxes, and drag coefficients in the marginal ice zone during the 1983 Marginal Ice Zone Experiment. *Journal of Geophysical Research*, 92(C7), 6921–6932.
- Fairall, C. W., White, A. B., Edson, J. B., & Hare, J. E. (1997). Integrated shipboard measurements of the marine boundary layer. *Journal of Atmospheric and Oceanic Technology*, 14, 338–359.
- Fofonoff, P., & Millard, R.C. Jr, (1983). Algorithms for computation of fundamental properties of seawater, 1983. Unesco Tech. Paper in Mar. Sci., No. 44, 53 pp.
- Grachev, A. A., Andreas, E. L., Fairall, C. W., Guest, P. S., & Persson, P. O. G. (2007). SHEBA flux-profile relationships in the stable atmospheric boundary layer. *Boundary-Layer Meteorology*, 124(3), 315–333. <https://doi.org/10.1007/s10546-007-9177-6>
- Groves, J. E., & Stringer, W. J. (1991). The use of AVHRR thermal infrared imagery to determine sea ice thickness within the Chukchi polynya. *Arctic*, 44, 130–139.
- Guanghua, H. A. O., & Jie, S. U. (2015). A study on the dynamic tie points ASI algorithm in the Arctic Ocean. *Acta Oceanologica Sinica*, 34(11), 126–135.
- Guest, P., Persson, P. O. G., Wang, S., Jordan, M., Jin, Y., Blomquist, B., & Fairall, C. (2018). Low-level baroclinic jets over the new Arctic Ocean. *Journal of Geophysical Research: Oceans*, 123. <https://doi.org/10.1002/2018JC013778>
- Häkkinen, S. (1986). Coupled ice-ocean dynamics in the marginal ice zones: Upwelling/downwelling and eddy generation. *Journal of Geophysical Research*, 91(C1), 819–832.
- Häkkinen, S. (1987). Feedback between ice flow, barotropic flow, and baroclinic flow in the presence of bottom topography. *Journal of Geophysical Research*, 92(C4), 3807–3820.
- Horvat, C., Tziperman, E., & Campin, J.-M. (2016). Interaction of sea ice floe size, ocean eddies, and sea ice melting. *Geophysical Research Letters*, 43, 8083–8090. <https://doi.org/10.1002/2016GL069742>
- Hutchings, J. K. (2018). Shipborne visual observations of Arctic sea ice. PANGAEA. <https://doi.org/10.1594/PANGAEA.889209>
- Inoue, J., & cruise participants (2014). The predictability study of the Arctic cyclones, R/V Mirai Cruise Report, JAMSTEC MR14–05, 239 pp.
- Inoue, J., & Hori, M. E. (2011). Arctic cyclogenesis at the marginal ice zone: A contributory mechanism for the temperature amplification? *Geophysical Research Letters*, 38, L12502. <https://doi.org/10.1029/2011GL047696>
- Jackson, J. M., Carmack, E. C., McLaughlin, F. A., Allen, S. E., & Ingram, R. G. (2010). Identification, characterization, and change of the near-surface temperature maximum in the Canada Basin, 1993–2008. *Journal of Geophysical Research*, 115, C05201. <https://doi.org/10.1029/2009JC005265>
- Kawaguchi, Y., Nishino, S., & Inoue, J. (2015). Fixed-point observation of mixed layer evolution in the seasonally ice-free Chukchi Sea: Turbulent mixing due to gale winds and internal gravity waves. *Journal of Physical Oceanography*, 45, 836–853.
- Lee, C., Thomson, J., & the Marginal Ice Zone and Arctic Sea State Teams (2017). An autonomous approach to observing the seasonal ice zone in the western Arctic. *Oceanography*, 30(2), 56–68. <https://doi.org/10.5670/oceanog.2017.222>
- Lund, B., Gruber, H. C., Persson, P. O. G., Smith, M., Doble, M., Thomson, J., et al. (2018). Arctic sea ice drift measured by shipboard marine radar. *Journal of Geophysical Research: Oceans*, 123. <https://doi.org/10.1029/2018JC013769>
- Lund, B., Zappa, C. J., Gruber, H. C., & Cifuentes-Lorenzen, A. (2017). Shipboard wave measurements in the Southern Ocean. *Journal of Atmospheric and Oceanic Technology*, 34(9), 2113–2126.
- Lüpkes, C., Gryanik, V. M., Hartmann, J., & Andreas, E. L. (2012). A parameterization, based on sea ice morphology, of the neutral atmospheric drag coefficients for weather prediction and climate models. *Journal of Geophysical Research*, 117, D13112. <https://doi.org/10.1029/2012JD017630>
- Lüpkes, C., Vihma, T., Jakobson, E., König-Langlo, G., & Tetzlaff, A. (2010). Meteorological observations from ship cruises during summer to the central Arctic: A comparison with reanalysis data. *Geophysical Research Letters*, 37, L09810. <https://doi.org/10.1029/2010GL042724>
- Maykut, G. A. (1982). Large-scale heat exchange and ice production in the Central Arctic. *Journal of Geophysical Research*, 87, 7971–7984.
- Overland, J. E. (1985). Atmospheric boundary layer structure and drag coefficients over sea ice. *Journal of Geophysical Research*, 90(C5), 9029–9049.
- Paluch, I. R., Lenschow, D. H., & Wang, Q. (1997). Arctic boundary layer in the fall season over open and frozen sea. *Journal of Geophysical Research*, 102(D22), 25,955–25,971.
- Perovich, D. K., & Polashenski, C. (2012). Albedo evolution of seasonal Arctic sea ice. *Geophysical Research Letters*, 39, L08501. <https://doi.org/10.1029/2012GL051432>
- Persson, P. O. G., Fairall, C. W., Andreas, E. L., Guest, P. S., & Perovich, D. K. (2002). Measurements near the atmospheric surface flux group tower at SHEBA: Near-surface conditions and surface energy budget. *Journal of Geophysical Research*, 107(C10), 8045. <https://doi.org/10.1029/2000JC000705>
- Persson, P. O. G., Hare, J. E., Fairall, C. W., & Otto, W. (2005). Air-sea interaction processes in warm and cold sectors of extratropical cyclonic storms observed during FASTEX. *Quarterly Journal of the Royal Meteorological Society*, 131, 877–912. <https://doi.org/10.1256/qj.03.181>
- Pinto, J. O. (1998). Autumnal mixed-phase cloudy boundary layers in the Arctic. *Journal of the Atmospheric Sciences*, 55, 2016–2038.
- Rinke, A., Maslowski, W., Dethloff, K., & Clement, J. (2006). Influence of sea ice on the atmosphere: A study with an Arctic atmospheric regional climate model. *Journal of Geophysical Research*, 111, D16103. <https://doi.org/10.1029/2005JD006957>
- Rudnick, D. L., & Klinck, J. (2007). The underway conductivity–temperature–depth instrument. *Journal of Atmospheric and Oceanic Technology*, 24, 1910–1923. <https://doi.org/10.1175/JTECH2100.1>

- Sato, K., Inoue, J., Kodama, Y.-M., & Overland, J. E. (2012). Impact of Arctic sea-ice retreat on the recent change in cloud-base height during autumn. *Geophysical Research Letters*, 39, L10503. <https://doi.org/10.1029/2012GL051850>
- Smith, M., Stammerjohn, S., Persson, O., Rainville, L., Liu, G., Perrie, W., et al. (2018). Episodic reversal of the autumn ice advance caused by release of ocean heat in the Beaufort Sea. *Journal of Geophysical Research: Oceans*, 123, 3164–3185. <https://doi.org/10.1002/2018JC013764>
- Smith, M., & Thomson, J. (2016). Scaling observations of surface waves in the Beaufort Sea. *Elementa*, 4. <https://doi.org/10.12952/journal.elementa.000097>
- Solomon, A., Shupe, M., Persson, P. O. G., & Morrison, H. (2011). Moisture and dynamical interactions maintaining decoupled Arctic mixed-phase stratocumulus in the presence of a humidity inversion. *Atmospheric Chemistry and Physics*, 11, 10,127–10,148. <https://doi.org/10.5194/acp-11-10127-2011>
- Sotropoulou, G., Tjernström, M., Sedlar, J., Achtert, P., Brooks, B. J., Brooks, I. M., et al. (2016). Atmospheric conditions during the Arctic Clouds in Summer Experiment (ACSE): Contrasting open-water and sea-ice surfaces during melt and freeze-up seasons. *Journal of Climate*, 29(24), 8721–8744. <https://doi.org/10.1175/JCLI-D-16-0211.1>
- Spreen, G., Kaleschke, L., & Heygster, G. (2008). Sea ice remote sensing using AMSR-E 89 GHz channels. *Journal of Geophysical Research*, 113, C02S03. <https://doi.org/10.1029/2005JC003384>
- Steele, M., & Ermold, W. (2015). Loitering of the retreating sea ice edge in the Arctic Seas. *Journal of Geophysical Research: Oceans*, 120, 7699–7721. <https://doi.org/10.1002/2015JC011182>
- Steele, M., Ermold, W., & Zhang, J. (2011). Modeling the formation and fate of the near-surface temperature maximum in the Canadian Basin of the Arctic Ocean. *Journal of Geophysical Research*, 116, C11015. <https://doi.org/10.1029/2010JC006803>
- Stroeve, J., Serreze, M. C., Holland, M. M., Kay, J. E., & Maslanik, J. (2012). The Arctic's rapidly shrinking sea ice cover: A research synthesis. *Climatic Change*, 110, 1005–1027.
- Thomson, J., Ackley, S., Girard-Ardhuin, F., Ardhuin, F., Babanin, A., Boutin, G., et al. (2018). Overview of the Arctic sea state and boundary layer physics program. *Journal of Geophysical Research: Oceans*. <https://doi.org/10.1002/2018JC013766>
- Timmermans, M.-L., Proshutinsky, A., Golubeva, E., Jackson, J. M., Krishfield, R., McCall, M., et al. (2014). Mechanisms of Pacific summer water variability in the Arctic's Central Canada basin. *Journal of Geophysical Research: Oceans*, 119, 7523–7548. <https://doi.org/10.1002/2014JC010273>
- Tjernström, M., Birch, C. E., Brooks, I. M., Shupe, M. D., Persson, P. O. G., Sedlar, J., et al. (2012). Meteorological conditions in the central Arctic summer during the Arctic Summer Cloud Ocean Study (ASCOS). *Atmospheric Chemistry and Physics*, 12, 1–27. <https://doi.org/10.5194/acp-12-1-2012>
- Tjernström, M., Leck, C., Persson, P. O. G., Jensen, M. L., Oncley, S. P., & Targino, A. (2004). The summertime Arctic atmosphere: Meteorological measurements during the Arctic Ocean Experiment 2001 (AOE-2001). *Bulletin of the American Meteorological Society*, 85, 1305–1321.
- Tjernström, M., Shupe, M. D., Brooks, I. M., Persson, P. O. G., Prytherch, J., Salisbury, D., et al. (2015). Warm-air advection, air mass transformation and fog causes rapid ice melt. *Geophysical Research Letters*, 42, 5594–5602. <https://doi.org/10.1002/2015GL064373>
- Uttal, T., Curry, J. A., McPhee, M. G., Perovich, D. K., Moritz, R. E., Maslanik, J. A., et al. (2002). The surface heat budget of the Arctic. *Bulletin of the American Meteorological Society*, 83, 255–275.
- Wadhams, P., Aulicino, G., Parmiggiani, F., Persson, P. O. G., & Holt, B. (2018). Pancake ice thickness mapping in the Beaufort Sea from wave dispersion observed in SAR imagery. *Journal of Geophysical Research: Oceans*, 123, 2213–2237. <https://doi.org/10.1002/2017JC013003>
- Wang, X., Key, J. R., & Liu, Y. (2010). A thermodynamic model for estimating sea and lake ice thickness with optical satellite data. *Journal of Geophysical Research*, 115, C12035. <https://doi.org/10.1029/2009JC005857>
- Wang, X., Key, J., Kwok, R., & Zhang, J. (2016). Comparison of Arctic sea ice thickness from satellites, aircraft, and PIOMAS data. *Remote Sensing*, 8, 713. <https://doi.org/10.3390/rs9090713>
- Waseda, T., Webb, A., Sato, K., Inoue, J., Kohout, A., Penrose, B., & Penrose, S. (2018). Correlated increase of high ocean waves and winds in the ice-free waters of the Arctic Ocean. *Scientific Reports*, 8, 4489. <https://doi.org/10.1038/s41598-018-22500-9>
- Yu, Y., & Rothrock, D. A. (1996). Thin ice thickness from satellite thermal imagery. *Journal of Geophysical Research*, 101(C10), 25,753–25,766.